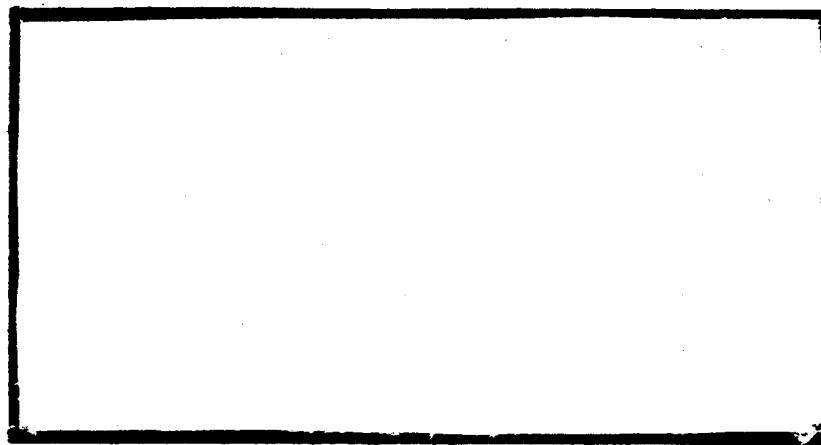


DTIC
ELECTE
JAN 05 1995
S G D



DEPARTMENT OF THE AIR FORCE
AIR UNIVERSITY
AIR FORCE INSTITUTE OF TECHNOLOGY

Wright-Patterson Air Force Base, Ohio

DISTRIBUTION STATEMENT A

Approved for public release;
Distribution Unlimited

19950103 070

AFIT/GE/ENG/94D-29

Accession For	
NTIS CRA&I	<input checked="checked" type="checkbox"/>
DTIC TAB	<input type="checkbox"/>
Unannounced	<input type="checkbox"/>
Justification _____	
By _____	
Distribution /	
Availability Codes	
Dist	Avail and/or Special
A-1	

Compensated Deconvolution from Wavefront Sensing

THESIS

Lori A. Thorson
Second Lieutenant, USAF

AFIT/GE/ENG/94D-29

DTIC QUALITY INSPECTED 3

Approved for public release; distribution unlimited

The views expressed in this thesis are those of the author and do not reflect the official policy or position of the Department of Defense or the U. S. Government.

AFIT/GE/ENG/94D-29

Compensated Deconvolution from Wavefront Sensing

THESIS

Presented to the Faculty of the School of Engineering
of the Air Force Institute of Technology

Air University

In Partial Fulfillment of the
Requirements for the Degree of
Master of Science in Electrical Engineering

Lori A. Thorson, BSEE
Second Lieutenant, USAF

Dec, 1994

Approved for public release; distribution unlimited

Acknowledgements

I'd like to thank my faculty co-advisor, Dr. Byron Welsh, for his assistance and encouragement throughout this project. His enthusiasm and his interest in this subject in this subject area were constant sources of inspiration.

I'd like to thank my other faculty co-advisor, Major Michael C. Roggemann, for his assistance in providing the computer code necessary in this thesis. His patience and help in understanding some of the concepts was detrimental to the completion of this thesis.

I'd also like to thank my sponsor, Dr. Brent Ellerbroek, for his cooperation in this thesis, which greatly contributed to the quality of this thesis.

Finally I'd like to thank my fellow AFIT students. Their sense of humor is the part of my AFIT experience that I will always remember.

Lori A. Thorson

Table of Contents

	Page
Acknowledgements	ii
List of Figures	vi
List of Tables	x
Abstract	xi
I. Introduction	1
1.1 Motivation	1
1.1.1 Terminology	2
1.1.2 Atmospheric Turbulence	3
1.1.3 Adaptive Optics	4
1.1.4 Conventional Deconvolution	6
1.1.5 Deconvolution from Wavefront Sensing (DWFS)	7
1.1.6 Compensated Deconvolution from Wavefront Sensing (CDWFS)	10
1.2 Problem Statement	11
1.3 Approach	11
1.4 Scope	12
1.5 Chapter Outline	12
1.5.1 Chapter 2	12
1.5.2 Chapter 3	12
1.5.3 Chapter 4	13
1.5.4 Chapter 5	13
1.6 Summary of Key Results	13

	Page
II. Background on CDWFS	14
2.1 Introduction	14
2.2 Estimators	14
2.3 Signal-to-Noise Considerations	16
2.4 Previous Simulation Results	18
2.5 Conclusion	19
III. Methodology	20
3.1 Introduction	20
3.2 Investigation of Extended Object Imaging Using CDWFS	21
3.2.1 Simulation Code	21
3.2.2 Extended Object Imaging	25
3.2.3 Performance Metric	26
3.2.4 Photon Levels	27
3.3 Conclusion	31
IV. Results	32
4.1 Introduction	32
4.1.1 System Parameters	33
4.2 Experiment one	35
4.2.1 Simulation Parameters	35
4.2.2 Simulation Results	35
4.2.3 Conclusion	41
4.3 Experiment two	42
4.3.1 Simulation Parameters	42
4.3.2 Simulation Results	42
4.3.3 Conclusion	48
4.4 Experiment three	49

	Page
4.4.1 Simulation Parameters	49
4.4.2 Simulation Results	49
4.4.3 Conclusion	60
4.5 Experiment four	61
4.5.1 Simulation Parameters	61
4.5.2 Simulation Results	61
4.5.3 Conclusion	62
4.6 Conclusion	68
V. Conclusions and Recommendations	69
5.1 Introduction	69
5.2 Conclusions	69
5.3 Recommendations for Further Research	71
Bibliography	72
Vita	74

List of Figures

Figure	Page
1. Average image captured by a partially compensated system with a 1-meter telescope, $m_\nu = 0.0$, and $\vec{vt} = 0$ cm.	7
2. Deconvolution performed on the average image captured by a partially compensated system	8
3. Function block diagram of the DWFS technique	9
4. Functional block diagram of a closed-loop adaptive-optics system that could be used for compensated deconvolution from wavefront sensing	10
5. Functional block diagram of a unfolded open-loop adaptive-optics system modeled in the compensated deconvolution from wavefront sensing work presented here	11
6. Functional block diagram of unfolded, open-loop adaptive-optics system modeled in the CDWFS work presented in this thesis.	21
7. Block diagram for simulation; \vec{vt} is defined in the text.	22
8. Wavefront sensor and mirror actuator geometry	23
9. Typical Space Satellite	34
10. Average CDWFS image (top left), average deconvolved image (top right), long exposure image (bottom left) and the radially averaged mean-square Fourier phase error (bottom right) with a delay time, vt , of 0 cm	36
11. Average CDWFS image (top left), average deconvolved image (top right), long exposure image (bottom left), and the radially averaged mean-square Fourier phase error (bottom right) with a delay time, vt , of 5 cm	37
12. Average CDWFS image (top left), average deconvolved image (top right), long exposure image (bottom left), and the radially averaged mean-square Fourier phase (bottom right) error with a delay time, vt , of 10 cm	38

Figure	Page
13. Average CDWFS image (top left), average deconvolved image (top right), long exposure image (bottom left), and the radially averaged mean-square Fourier phase error (bottom right) with a delay time, vt , of 20 cm	39
14. Radially averaged mean-square Fourier phase errors for the average CDWFS images (top) and the deconvolution images (bottom) with delay time of 0 cm, 5 cm, 10 cm and 20 cm	40
15. Average CDWFS image (top left), average deconvolved image (top right), long exposure image (bottom left), and the radially averaged mean-square Fourier phase error (bottom right) with a delay time, vt , of 0 cm	43
16. Average CDWFS image (top left), average deconvolved image (top right), long exposure image (bottom left), and the radially averaged mean-square Fourier phase error (bottom right) with a delay time, vt , of 5 cm	44
17. Average CDWFS image (top left), average deconvolved image (top right), long exposure image (bottom left), and the radially averaged mean-square Fourier phase error (bottom right) with a delay time, $\vec{v}\vec{t}$, of 10 cm	45
18. Average CDWFS image (top left), average deconvolved image (top right), long exposure image (bottom left), and the radially averaged mean-square Fourier phase error (bottom right) with a delay time, vt , of 20 cm	46
19. Radially averaged mean-square Fourier phase errors for the average CDWFS images (top) and the deconvolution images (bottom) with delay time of 0 cm, 5 cm, 10 cm and 20 cm	47
20. Average CDWFS image (top left), average deconvolved image (top right), long exposure image (bottom left), and the radially averaged mean-square Fourier phase error (bottom right) with a visual magnitude, m_ν , of 0.0 and $\vec{v}\vec{t} = 0$ cm	51

Figure	Page
21. Average CDWFS image (top left), average deconvolved image (top right), long exposure image (bottom left), and the radially averaged mean-square Fourier phase error (bottom right) with a visual magnitude, m_ν , of 1.0 and $\vec{vt} = 0$ cm	52
22. Average CDWFS image (top left), average deconvolved image (top right), long exposure image (bottom left), and the radially averaged mean-square Fourier phase error (bottom right) with a visual magnitude, m_ν , of 2.0 and $\vec{vt} = 0$ cm	53
23. Average CDWFS image (top left), average deconvolved image (top right), long exposure image (bottom left), and the radially average mean-square Fourier phase error (bottom right) with a visual magnitude, m_ν , of 3.0 and $\vec{vt} = 0$ cm	54
24. Average CDWFS image (top left), average deconvolved image (top right), long exposure image (bottom left), and the radially averaged mean-square Fourier phase error (bottom right) with a visual magnitude, m_ν , of 4.0 and $\vec{vt} = 0$ cm	55
25. Average CDWFS image (top left), average deconvolved image (top right), long exposure image (bottom left), and the radially averaged mean-square Fourier phase error (bottom right) with a visual magnitude, m_ν , of 5.0 and $\vec{vt} = 0$ cm	56
26. Average CDWFS image (top left), average deconvolved image (top right), long exposure image (bottom left), and the radially averaged mean-square Fourier phase error (bottom right) with a visual magnitude, m_ν , of 6.0 and $\vec{vt} = 0$ cm	57
27. Average CDWFS image (top left), average deconvolved image (top right), long exposure image (bottom left), and the radially averaged mean-square Fourier phase error (bottom right) with a visual magnitude, m_ν , of 7.0 and $\vec{vt} = 0$ cm	58
28. Average CDWFS image (top left), average deconvolved image (top right), long exposure image (bottom left), and the radially averaged mean-square Fourier phase error (bottom right) with a visual magnitude, m_ν , of 8.0 and $\vec{vt} = 0$ cm	59

Figure	Page
29. Average CDWFS image (top left), average deconvolved image (top right), long exposure image (bottom left), and the radially averaged mean-square Fourier phase error (bottom right) with a visual magnitude, m_ν , of 0.0 and $\vec{v}\vec{t} = 10$ cm	63
30. Average CDWFS image (top left), average deconvolved image (top right), long exposure image (bottom left), and the radially averaged mean-square Fourier phase error (bottom right) with a visual magnitude, m_ν , of 5.0 and $\vec{v}\vec{t} = 10$ cm	64
31. Average CDWFS image (top left), average deconvolved image (top right), long exposure image (bottom left), and the radially averaged mean-square Fourier phase error (bottom right) with a visual magnitude, m_ν , of 7.0 and $\vec{v}\vec{t} = 10$ cm	65
32. Average CDWFS image (top left), average deconvolved image (top right), long exposure image (bottom left), and the radially averaged mean-square Fourier phase error (bottom right) with a visual magnitude, m_ν , of 8.0 and $\vec{v}\vec{t} = 10$ cm	66
33. Radially averaged mean-square Fourier phase errors for the average CDWFS images (top) and the deconvolution images (bottom) with visual magnitudes m_ν of 0.0, 5.0, 7.0, and 8.0 and $\vec{v}\vec{t} = 10$ cm	67

List of Tables

Table		Page
1.	Photon flux values for the image with $\lambda_{img} = 0.7\mu\text{m}$, $\tau = 0.1$, BW = 10%	28
2.	Simulation parameters used in the calculation of K_I and K_W	29
3.	Photon flux values for the WFS with $\lambda_{img} = 0.6\mu\text{m}$, $\tau = 0.1$, BW = 20%	30
4.	K_I and K_W calculated from photon flux values	30

Abstract

The U.S. Air Force has a continuing mission to obtain imagery of earth-orbiting objects. One of the means for obtaining this imagery is through the use of ground-based observatories. A fundamental problem associated with imaging objects through the atmosphere is that atmospheric turbulence inflicts a large, random aberration on the telescope which effectively limits the realizable resolution to that of a much smaller telescope. Several approaches have been taken to overcome these effects including pure post processing, pure adaptive optics, and hybrid techniques involving both adaptive optics and image post processing. One key result from past approaches is that partially compensated systems can be used in conjunction with image processing to overcome most of the optical effects of atmospheric turbulence while retaining nearly the performance of a fully compensated system. One hybrid approach is compensated deconvolution from wavefront sensing (CDWFS). This method uses wavefront sensor measurements in conjunction with short exposure images to improve the effective optical performance. This thesis formulates and executes a plan which allows fundamental questions regarding partially compensated adaptive optics performance to be answered. Specifically, imaging of extended objects using the CDWFS technique is investigated, through simulation. The simulation results demonstrate that the CDWFS technique can be used to reduce the required closed-loop bandwidth of an imaging system, permitting longer integration times in the wavefront sensor, and thus allowing dimmer objects to be imaged without the use of an artificial guidestar.

Compensated Deconvolution from Wavefront Sensing

I. Introduction

1.1 Motivation

The Air Force has a continuing mission to obtain imagery of earth-orbiting objects. One of the means for obtaining this imagery is through the use of ground-based observatories. A fundamental problem associated with imaging objects through the atmosphere is that atmospheric turbulence inflicts a large, random aberration on the telescope which effectively limits the realizable resolution to that of a much smaller telescope. Three methods have been presented in the literature to lessen the effects of atmospheric turbulence on ground-based telescope systems. These methods encompass the use of both hardware and software and include pure image post processing [3, 7, 22, 24], pure adaptive optics [10, 25], and hybrid techniques involving both adaptive optics and image post processing [18, 19]. Hybrid approaches trade adaptive optics complexity for post detection image processing. The theory for these techniques has been developed. One key result is that partially compensated systems can be used in conjunction with image processing to overcome most of the optical effects of atmospheric turbulence while retaining nearly the performance of a fully compensated system. One specific hybrid approach is compensated deconvolution from wavefront sensing (CDWFS). This chapter provides the background necessary to understand the fundamental problem of atmospheric turbulence, its effect on Air Force adaptive optical imaging systems, and the use of CDWFS as a post processing technique to improve image quality. The theory for this technique is presented and this thesis will investigate imaging of extended objects, through simulation, using the CDWFS technique.

1.1.1 Terminology. Defining the basic terms and concepts is the first step in understanding the theory. The following terms will be used throughout the remainder of this investigation.

Phase screen: A phase screen changes the phase of an incident optical field in an unpredictable fashion (random).

Subapertures: Subapertures are small regions in the telescope pupil where gradients in the phase aberration are measured.

Deformable mirror: A flexible mirror whose surface figure can be modified at high speeds in response to applied electrical signal.

Actuators: Electrical device on the deformable mirror that changes the figure of the mirror.

Scintillation: Scintillation is amplitude aberrations in the wavefront. This becomes an factor when the atmospheric turbulence is strong.

Hartmann sensor: A wavefront sensing device that measures gradients in the phase aberration across the telescope pupil.

Photoevents: The creation of a free electron in the detector is called a photoevent.

Influence functions: The functions that are applied to the deformable mirror by the actuators. In simulations, these are modeled as Gaussian functions.

Residual wavefront error: Aberrations left in the wavefront after passing through an adaptive optics system.

Optical transfer function (OTF): The transfer of frequency components of object intensity to image intensity by the imaging system.

Extended objects: Objects that have width, such as satellites.

The next section discusses atmospheric turbulence and its effects on optical systems.

1.1.2 Atmospheric Turbulence. Atmospheric turbulence imposes a severe and fundamental limit to the resolution of ground-based telescopes [11]. Turbulent motion in the atmosphere causes random variations in the index of refraction of the atmosphere, resulting in random phase aberrations appearing in the pupil of the telescope. These random aberrations cause the limiting resolution of conventional imaging systems to be imposed by the atmosphere, rather than by the size and optical design of a large telescope.

Astronomers and others concerned with the propagation of light waves through turbulence have developed various parameters for characterizing the severity of image degradation due to turbulence. Astronomers typically use such parameters to compare the relative seeing quality of candidate sites for new observatories. One of the most convenient and widely used measures of seeing quality was introduced by Fried [2] and is denoted r_o , the atmospheric coherence diameter. It is defined as the effective diameter of a telescope for which the integral of the telescope's optical transfer function is equal to the ensemble averaged atmospheric optical transfer function [12]. The parameter r_o is a function of the zenith angle of the propagation path, the wavelength, and the strength of the turbulence [12]. Typical values for r_o at visible wavelengths at a good observatory range from 5 cm for poor seeing to 20-40 cm for exceptional seeing [6]. In addition to its practical use as a measure of relative seeing quality, r_o is widely used in expressions for the atmospheric optical transfer function to simplify the forms of these expressions, and to aid in understanding their behavior [6].

A number of techniques have been proposed for compensating the effects of atmospheric turbulence. Pure post processing techniques use specialized image measurements and statistical image-processing algorithms to improve resolution. Pure predetection correction is accomplished by means of adaptive optics. Hybrid techniques combine elements of predetection correction and post detection image reconstruction to compensate for atmospheric turbulence. This thesis investigates the

imaging of extended objects using a particular hybrid technique: compensated deconvolution from wavefront sensing (CDWFS). The following sections present a brief overview of adaptive optics systems, followed by a discussion of deconvolution and deconvolution from wavefront sensing (DWFS) and finally introducing the CDWFS technique.

1.1.3 Adaptive Optics. The notion that aberrations induced by the atmosphere could be compensated using mechanical means was first put forth by Babcock [1]. Babcock's conjecture arose from the realization that the physical origin of the turbulence-induced aberration is spatial variations in the optical path length between the object and the telescope. If these optical path length differences could be mechanically compensated before the light is focused into an image and detected then the measured image will be superior to an uncompensated image. Systems which perform turbulence compensation using mechanical means now exist, and are generically referred to as adaptive optics systems [7, 8]. Adaptive optics provide a means of sensing the atmospheric turbulence-induced aberration and, at least partially, correcting for this aberration in real time. Image quality is improved by reducing the aberration caused by the atmosphere and results in improved resolution.

The key elements of an adaptive optics system include the deformable mirror (DM), the wavefront sensor (WFS), and an actuator command computer. The DM is a flexible mirror whose surface figure can be modified at high speed in response to applied electrical signals. Voltages applied to the actuators cause them to expand or contract, resulting in a change to the figure of the mirror surface. The WFS is a device which measures gradients in the phase aberration across small regions in the telescope pupil, called subapertures. The DM, WFS, and actuator command computer are arranged in a closed-loop system. Aberrated light entering the telescope is first reflected from the deformable mirror. Some of this light is focused to form an image, and some is used to provide signal to the WFS. The actuator command computer processes WFS measurements, and calculates the set of electrical signals

to apply to the DM to achieve the desired DM figure. The entire process, from WFS measurement to DM update, must be performed at speeds commensurate with the rate of change of the turbulence-induced phase errors. In an ideal adaptive optics system the surface of the DM is configured from instant to instant to present an approximation to the conjugate of the turbulence-induced phase error so that the wave reflected from the DM will more closely approximate a plane wave.

The fundamental limitations of an adaptive optics system are the accuracy of the wavefront sensors, the finite number of wavefront sensors employed across the wavefront surface, the finite number of degrees-of-freedom in the deformable mirror's response, and the finite system response time [24]. Photon noise imposes a limit on the accuracy of the wavefront sensors. At low light levels, shot noise and measurement noise effects in the wavefront sensor impose an additional limitation on sensor accuracy and seriously degrade the reconstruction process. The finite number of sensors employed by an adaptive optics system also limits the accuracy of the wavefront measurement. The finite number of degrees-of-freedom in the deformable mirror limits the device's response such that higher-order wavefront aberrations cannot be corrected. The rapid fluctuations in the phase aberrations demand that the reconstruction computations be performed at a rate of approximately one frame per millisecond at visible wavelengths. Because of these limitations, residual phase errors exist in the wavefront propagating from the deformable mirror, and these phase errors degrade the resulting image by scattering a fraction of the incident power through various random angles [21]. Hence, adaptive optics systems are incapable of fully compensating for phase aberrations. To obtain the highest level of optical performance for large telescopes operating at visible wavelengths adaptive-optics systems can require several hundred to a few thousand wavefront subapertures and deformable mirror actuators. As a consequence, simpler adaptive-optics systems have been explored and are referred to as partially compensated adaptive-optics systems.

The expense and complexity of adaptive-optics systems has motivated an investigation into partially compensated adaptive-optics systems [13, 20, 23]. These systems use fewer, larger WFS subapertures and fewer DM degrees-of-freedom. Partially compensated adaptive-optics systems are defined here as systems that have wavefront sensor subapertures that are bigger than the atmospheric coherence diameter r_o , have deformable mirror actuators that are separated by more than r_o , or both. Adaptive-optics systems that operate in the infrared region of the spectrum take advantage of the fact that the relative seeing, as measured by D/r_o , where D is the telescope diameter, is much more favorable at longer wavelengths. However, the diffraction-limited angular resolution is much poorer at infrared wavelengths. This consideration drives military systems toward operation in the visible band of the spectrum, while astronomical systems are being designed primarily for infrared operation.

Partially compensating systems are of interest because if the image-measurement process is treated as being part of an image reconstruction problem, then it is possible to obtain an excellent signal-to-noise (SNR) for high spatial frequencies with partially compensating systems [15, 18]. Some type of post processing, however, is required for partially compensating systems because the high spatial frequencies are highly attenuated by the telescope-adaptive optics-atmosphere system. Deconvolution has been successfully used to boost the high spatial frequencies in images measured with a partially compensated adaptive-optics system [16].

1.1.4 Conventional Deconvolution. Conventional deconvolution has been shown to successfully enhance images measured by partially compensated adaptive-optics systems. Conventional deconvolution uses an average OTF obtained from a reference source and an average image to produce the deconvolved image. The atmosphere-adaptive-optics partially compensated imaging system heavily attenuates high spatial frequencies. Figure 1 shows an example of an average image captured by a partially compensated system. The attenuation of high spatial frequencies

(blurring) is clearly seen in this figure. Conventional deconvolution attempts to cor-

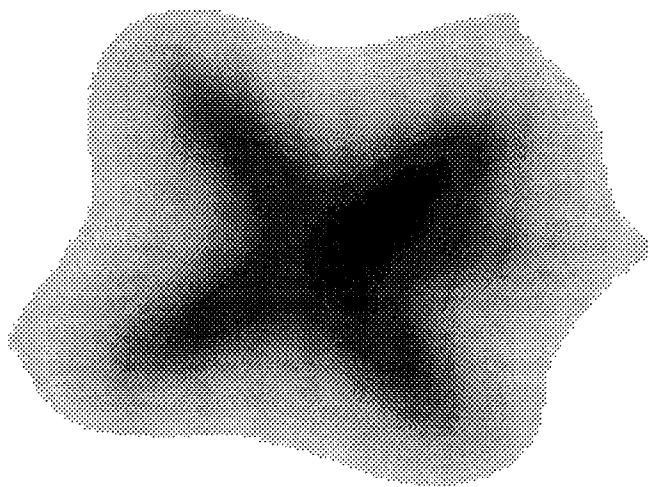


Figure 1. Average image captured by a partially compensated system with a 1-meter telescope, $m_v = 0.0$, and $\vec{vt} = 0$ cm.

rect for this blurring by recovering the high spatial frequencies with the use of an inverse filtering technique. Figure 2 shows the average image after conventional deconvolution. The image has been enhanced by increasing the high spatial frequency content. Conventional deconvolution, however, has an inherent problem of boosting high spatial frequency noise as well as the high spatial frequency content of the image. If a technique can be developed such that the OTF can be calculated for each realization, the object spectrum could be estimated for each realization and averaged over the total number of frames. This would alleviate the need to use of the inverse filter and would prevent high spatial frequency noise from being introduced.

1.1.5 Deconvolution from Wavefront Sensing (DWFS). One such technique that has been developed meets this criterion, deconvolution from wavefront sensing (DWFS). Figure 3 shows the functional diagram of the DWFS technique. In addition to an imaging camera, a wavefront sensor is conjugated with the entrance pupil in order to determine the wavefront at the same time that the image is determined.



Figure 2. Deconvolution performed on the average image captured by a partially compensated system

This approach makes it possible to obtain the OTF for each realization. Hence the spatial frequencies that have not completely disappeared from the image can be corrected. The lost spatial frequencies are different for each realization because of the randomness of the atmosphere. From this the entire frequency spectrum of the object can be restored from a sufficiently large set of short-exposure images and corresponding wavefronts. Equation (1) shows the estimator used to calculate estimated object spectrum,

$$\tilde{O}(u, v) = \frac{I(u, v) \langle \tilde{H}^*(u, v) \rangle}{\langle |\tilde{H}(u, v)|^2 \rangle} \quad (1)$$

where $\tilde{O}(u, v)$ is the estimated object spectrum, $I(u, v)$ is the image spectrum, $\tilde{H}(u, v)$ is the estimated OTF. The estimated object is then found by inverse Fourier transforming the estimated object spectrum. Because all spatial frequencies can potentially be obtained with a large set of images/wavefronts, DWFS can provide reconstructed images without the high spatial frequency noise inherent with conventional deconvolution.

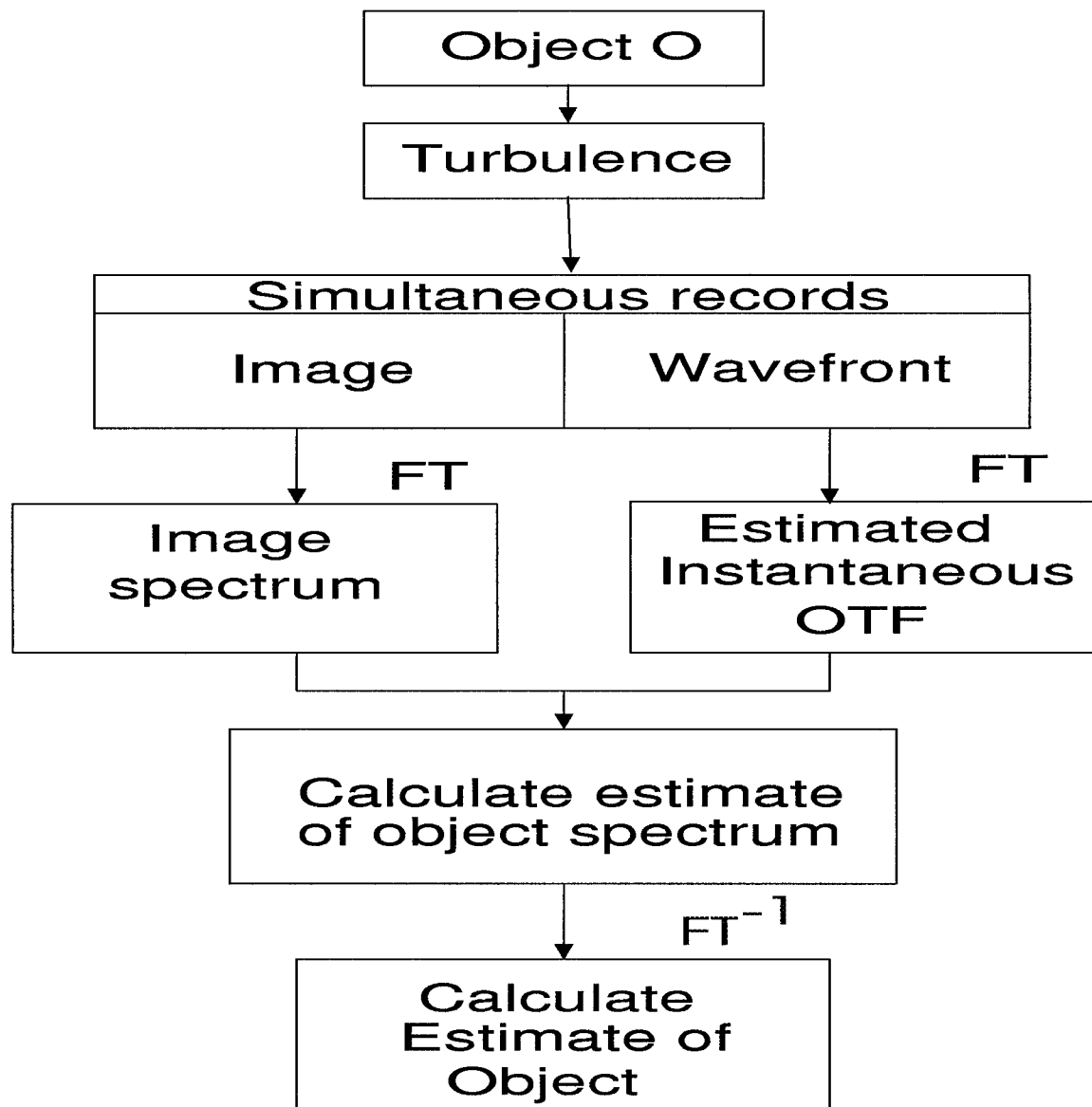


Figure 3. Function block diagram of the DWFS technique

1.1.6 Compensated Deconvolution from Wavefront Sensing (CDWFS).

The use of an alternative image-reconstruction process is explored for reconstructing images captured by partially compensated imaging systems. A functional block diagram of a closed-loop adaptive-optics system that could be used to perform compensated deconvolution from wavefront sensing is shown in Figure 4. To avoid the analytic and computational complexities associated with deformable mirror dynamics, the unfolded, open-loop version of the adaptive-optics system, shown in Figure 5, is used to obtain the results presented here. Wavefront sensor measurements available in open-loop adaptive-optics imaging system are used to perform post processing. These measurements can be used to improve the instantaneous compensated optical transfer function (OTF) under some conditions. Of necessity, this method uses short-exposure image measurements and simultaneous measurements from a wavefront sensor. The method proposed is derived from DWFS and will, for purposes here, be referred to as compensated deconvolution from wavefront sensing (CDWFS).

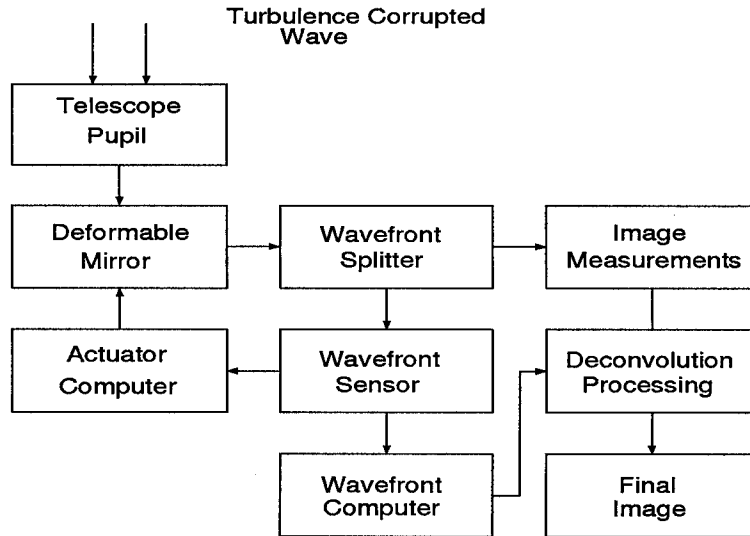


Figure 4. Functional block diagram of a closed-loop adaptive-optics system that could be used for compensated deconvolution from wavefront sensing

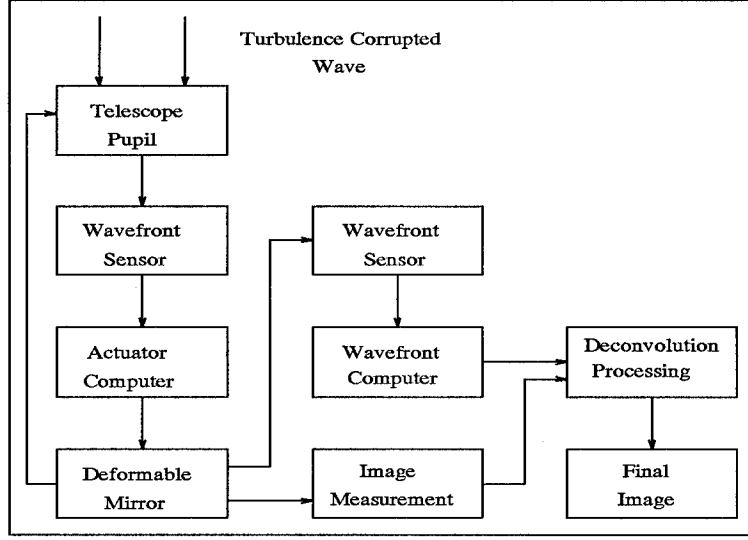


Figure 5. Functional block diagram of a unfolded open-loop adaptive-optics system modeled in the compensated deconvolution from wavefront sensing work presented here

1.2 Problem Statement

This thesis investigates compensated deconvolution from wavefront sensing (CDWFS). Through simulation, the CDWFS technique is evaluated for imaging extended objects. The image spectrums from the CDWFS technique will be compared to the conventional deconvolution using the mean-square Fourier phase error as the performance metric between each of these spectrums and the actual object spectrum.

1.3 Approach

This thesis addresses the problem statement by investigating the use of the CDWFS technique to improve optical performance. Specifically, the simulation code used in reference [14] is modified to include the imaging of extended objects. Comparisons are made between the CDWFS results and the conventional deconvolution results. The mean-square Fourier phase error is used as the performance metric in comparing these techniques.

This research effort employs a computer simulation as the primary research tool. The simulation code used by [14] is modified to include imaging of extended objects. The imaging package, HYSIM, is used to produce the results from the conventional deconvolution technique.

1.4 Scope

This thesis analyzes the performance of CDWFS employed as a post processing technique for an adaptive optics system. The primary parameters are the time delays in the closed-loop adaptive-optics system, the atmospheric seeing conditions, the light level for the image and the light level for the WFS. As a final product, this thesis contrasts the CDWFS technique results with the conventional deconvolution results. The mean-square Fourier phase error is the performance metric used in this comparison. The average CDWFS image and the average deconvolution image are also produced to show the degree of improvement of the CDWFS image.

1.5 Chapter Outline

The following is a brief review of the information found in each chapter of the thesis.

1.5.1 Chapter 2. This chapter presents a brief overview of CDWFS as a post processing technique to improve image quality. The theory of CDWFS is described in detail. The concepts presented in this chapter provide the ground work for the methodology developed in chapter 3.

1.5.2 Chapter 3. This chapter develops a detailed methodology for conducting the investigation, based on the background knowledge presented in Chapter 2. The approach used to image extended objects through simulation, is presented for both the CDWFS and the deconvolution techniques.

1.5.3 Chapter 4. This chapter presents the simulation results designed to explore the implementation of CDWFS as a post processing technique. The simulated results of imaging extended objects with the CDWFS technique and the deconvolution technique are presented and discussed.

1.5.4 Chapter 5. This chapter states the conclusions based upon the results presented in Chapter 4. Chapter 5 concludes with recommendations concerning the implementation of CDWFS as a post processing technique.

1.6 Summary of Key Results

The CDWFS technique outperforms the conventional deconvolution technique in all cases when the mean-square Fourier phase error is used as the performance metric. Both techniques are evaluated under the same conditions. Under average seeing conditions, the CDWFS technique introduces small Fourier phase errors compared to the large Fourier phase errors introduced with conventional deconvolution when the delay time in the closed-loop system is increased. When the seeing conditions are "poor", the CDWFS technique continues to provide reconstructed images with smaller Fourier phase errors than conventional deconvolution. The use of longer delay times implies that the bandwidth of operation can be reduced. This reduction of the closed-loop bandwidth permits longer integration times in the WFS, which then allows dimmer objects to be imaged without the use of an artificial guide star.

II. Background on CDWFS

2.1 Introduction

The theory for compensated deconvolution from wavefront sensing (CDWFS) has been published and has, through simulation, been verified. This chapter discusses the use of an estimator in the image reconstruction technique, CDWFS, to improve optical performance. The performance metrics, signal-to-noise ratio (SNR) and optical transfer function (OTF), are discussed for this estimator. These metrics are used in [14] in evaluating the CDWFS technique.

2.2 Estimators

Treating the image measurement process as part of an image reconstruction problem allows improvement in the performance of partially compensating systems [15, 18]. The DWFS estimator for the object spectrum is [4, 10, 25]

$$\tilde{O}(u) = \frac{\langle I(u)\tilde{H}^*(u) \rangle}{\langle |\tilde{H}(u)|^2 \rangle}, \quad (2)$$

where $\tilde{O}(u)$ is the estimated object spectrum, $I(u)$ is the instantaneous measured image spectrum, $\tilde{H}(u)$ is the estimated instantaneous OTF, and $\langle \rangle$ is used to represent the ensemble-averaging operation. The superscript $*$ represents the complex conjugate operator. It is assumed that $\tilde{H}(u)$ is obtained from the wavefront sensor measurements of the residual phase error in the pupil of the telescope. Equation (2) can be rewritten using the relationship $I(u) = O(u)H(u)$:

$$\tilde{O}(u) = \frac{O(u)\langle H(u)\tilde{H}^*(u) \rangle}{\langle |\tilde{H}(u)|^2 \rangle}, \quad (3)$$

where $H(u)$ is the actual instantaneous OTF and $O(u)$ is the object spectrum. Given Equation (3) the DWFS transfer function $S(u)$ can be defined as [25]

$$\langle S(u) \rangle = \frac{\tilde{O}(u)}{O(u)} = \frac{\langle H(u) \tilde{H}^*(u) \rangle}{\langle |\tilde{H}(u)|^2 \rangle}. \quad (4)$$

The numerator of Equation (4) attenuates the spatial frequencies of $O(u)$, since the $\tilde{H}^*(u)$ and $H(u)$ factors have a modulus less than one. The numerator also provides a degree of phase correction to the compensated OTF. The denominator of Equation (4) boosts the high spatial frequencies to account for attenuation caused by the numerator.

It should be noted that in uncompensated imaging, the first moments, $\langle H(u) \rangle$ and $\langle \tilde{H}(u) \rangle$, are extremely small for angular frequencies higher than r_o/λ [6], where λ is the mean wavelength of operation. This fact motivates the use of the second moment, $\langle |H(u)|^2 \rangle$, since it is well known that the second moment has useful values even at high spatial frequencies [6, 11].

It has been shown that for adaptive optical systems, including partially compensated systems, the average compensated OTF has useful values at high spatial frequencies [13, 15, 17, 20, 23]. Under these conditions it is useful to investigate techniques for correcting the phase of the compensated OTF to improve the effective imaging performance. A modification of the DWFS estimator is used for CDWFS, specifically,

$$\tilde{O}(u) = \langle I(u) \frac{\tilde{H}^*(u)}{|\tilde{H}(u)|} \rangle, \quad (5)$$

$$\tilde{O}(u) = O(u) \langle H(u) \frac{\tilde{H}^*(u)}{|\tilde{H}(u)|} \rangle. \quad (6)$$

The CDWFS estimator provides phase correction to the compensated OTF $H(u)$ by virtue of the fact that the term $\tilde{H}^*(u)/|\tilde{H}(u)|$ is a unit phasor, which in the limit of perfect estimation of the residual aberration has the conjugate of the phase of $H(u)$.

The CDWFS transfer function can be written as

$$\langle S(u) \rangle = \langle H^i(u) \frac{\tilde{H}^*(u)}{|\tilde{H}(u)|} \rangle. \quad (7)$$

It should be noted that $S(u)$ is not linearly related to the residual phase errors in the pupil of the telescope because there is not a linear relationship between the residual phase errors in the pupil of the telescope and the phase of the compensated OTF. Because of the nonlinearity, all the statistical quantities that need to be calculated are extremely difficult to obtain. For example, the first moment of the CDWFS estimator is a four-dimensional integral [25]. The second moment, required for the SNR analysis, is thus an eight-dimensional integral. Since the CDWFS estimator is not a linear function of the residual phase errors in the pupil of the telescope, an analytic expression cannot be evaluated for $S(u)$. Use of the estimator in Equation (5) permits direct comparison between the CDWFS transfer function and the average compensated OTF. Because of the difficulty associated with analytically calculating some of the statistical quantities required for prediction of the performance of CDWFS, a realistic simulation is used to compute all statistical quantities in the analysis. Section 3.2.1 discusses this simulation in detail.

2.3 Signal-to-Noise Considerations

The quality of a statistical estimator is typically characterized by a signal-to-noise ratio (SNR). The SNR is defined as [6]

$$SNR = \frac{\text{mean}}{\sqrt{\text{variance}}} \quad (8)$$

where the *mean* and *variance* are the quantities of interest. When a complex quantity is to be estimated, such as $Z(u)$, the definition of the SNR generalizes to the

real-valued function [9]

$$SNR(u) = \frac{|\langle Z(u) \rangle|}{\sqrt{\text{var}[Z(u)]}}, \quad (9)$$

where

$$\text{var}[Z(u)] = \langle |Z(u)|^2 \rangle - |\langle Z(u) \rangle|^2. \quad (10)$$

To analyze the SNR of $\tilde{O}(u)$, it must be noted that the signal at the image plane is a random process governed by Poisson statistics and that the transfer function $S(u)$ is also a random process governed by the statistics of the compensated OTF and the estimation process for the residual phase error. Such processes are referred to as doubly stochastic Poisson random processes [6]. The standard methods for analyzing doubly stochastic Poisson random processes can be used to show that the SNR of $\tilde{O}(u)$, $SNR(u)$, for a single frame $SNR(u)$ is given by [6, 9, 15, 18]

$$SNR(u) = \frac{K|O_n(u)||S(u)|}{[K + K^2|O_n(u)|^2\text{var}[S(u)] + Q_{IM}\sigma_{rms}^2]^{1/2}}, \quad (11)$$

where $O_n(u)$ is the object spectrum normalized to have a value of unity at $u = 0$, K is the average number of photoevents per image, Q_{IM} is the number of pixels in the image, and σ_{rms} is the rms number of read-noise electrons per pixel in a CCD detector. Similarly, for the case of short-exposure image measurements the SNR for the compensated image measurement, $SNR^{SE}(u)$, is given by [15]

$$SNR^{SE}(u) = \frac{K|O_n(u)||H(u)|}{[K + K^2|O_n(u)|^2\text{var}[H(u)] + Q_{IM}\sigma_{rms}^2]^{1/2}}, \quad (12)$$

If a sufficiently long exposure is used to allow $H(u)$ to approach its average value during the length of the exposure, then the long-exposure image spectrum SNR, $SNR^{LE}(u)$, is

$$SNR^{LE}(u) = \frac{K|O_n(u)||H(u)|}{\sqrt{K + Q_{IM}\sigma_{rms}^2}} \quad (13)$$

Averaging improves the SNR in the standard way [6]

$$SNR_N(u) = \sqrt{N}SNR(u), \quad (14)$$

where $SNR(u)$ is the expected single frame SNR and N is the number of realizations averaged.

2.4 Previous Simulation Results

Previous investigations of the CDWFS technique evaluated the performance for star imagery. The CDWFS transfer function was calculated with the use of Equation (5). The average compensated transfer function is found in the same way. Once averaged, these two transfer functions are compared. The first comparison is for various finite times required for computing and applying actuator commands which result in a delay between sensing and correcting for a realization of a residual phase error. This residual phase error changes from instant to instant. The resulting shape of the deformable mirror does not match the conjugate of the actual instantaneous aberration. Rather, the shape matches the conjugate of a slightly earlier version of the turbulence-corrupted wave front, reducing the average-compensated OTF. The results show that the CDWFS transfer function has no advantage over average compensated OTF when the delay times are small. However, as the delays get larger, the CDWFS transfer function is greater than the average compensated transfer function at mid and high spatial frequencies. This improvement allows the bandwidth to be reduced and permits longer integration times in the WFS. Dimmer objects can then be imaged without the use of an artificial guidestar.

The second comparison is made with the SNR of the CDWFS transfer function and the SNR of the short-exposure compensated OTF by using Equations (11) and (12), respectively. By this metric, the CDWFS estimator is less noisy than the

compensated OTF. Although the SNR's are sensitive to the spatial sampling of the residual wavefront, the CDWFS estimator is superior to the compensated OTF.

Finally, the spectral estimation of the image spectrum SNR's for the compensated image and for the CDWFS image are calculated. CDWFS provides improved estimation of the spectral components of an image when compared with compensated imaging alone. Higher effective cutoff spatial frequencies can also be achieved with CDWFS. The higher spatial frequency content, in turn, translates to higher effective resolution of an imaging system.

2.5 Conclusion

Atmospheric turbulence imposes a fundamental limit on the performance of any optical system. Adaptive optics systems are unable to fully compensate for the effects of atmospheric turbulence resulting in residual phase errors that degrade image quality. This thesis investigates the use of a post processing technique, CDWFS, to improve the quality of images measured by Air Force adaptive optics systems. The next chapter develops the methodology for conducting this investigation.

III. Methodology

3.1 Introduction

Chapter II provided an overview of the problem of imaging through the turbulent atmosphere. The Air Force employs adaptive optics systems to compensate for the random phase fluctuations which result from atmospheric turbulence. Earlier research [24] established that adaptive optics systems cannot fully compensate for these phase aberrations, which means that residual phase errors exist in the wavefront leaving the deformable mirror. These residual phase errors significantly degrade the images measured by an adaptive optics system, so additional processing is needed to improve image quality. Roggemann and Meinhardt [14] have shown through simulation that compensated deconvolution from wavefront sensing (CDWFS) can be used as a post processing technique to minimize the effects of residual phase errors in adaptive optics systems. The investigation presented in reference [14] used star imagery in evaluating the CDWFS technique. The average compensated OTF was compared to the average compensated CDWFS transfer function. The SNR's of each transfer function were also compared in this work. The Air Force, however, needs to image extended objects, such as satellites, with high resolution. This thesis extends the work done by Roggemann and Meinhardt [14] by investigating the performance of CDWFS for extended objects. This chapter begins by describing the simulation code used by [14]. Modifications to include imaging of extended objects with the CDWFS technique are discussed. Deconvolution is addressed to provide results from the conventional technique with which to compare the CDWFS results. Computer generated photon values are used in both simulations to simulate imaging of objects of varying visual magnitudes. This thesis also uses a different metric, from that used previously, to compare the CDWFS results and the deconvolution results. This new metric is the mean-square Fourier phase error.

3.2 Investigation of Extended Object Imaging Using CDWFS

The simulation code used by Roggemann and Meinhardt [14] is used here with modifications for imaging extended objects. Computer generated photon values and the mean-square Fourier phase error are addressed.

3.2.1 Simulation Code. Elements of the simulation have been carefully validated [17] and have been used in previous studies [18]. The functional block diagram of the unfolded, open-loop adaptive-optics modeled in the simulation is shown in Figure 6. The simulation block diagram is shown in Figure 7. A setup proce-

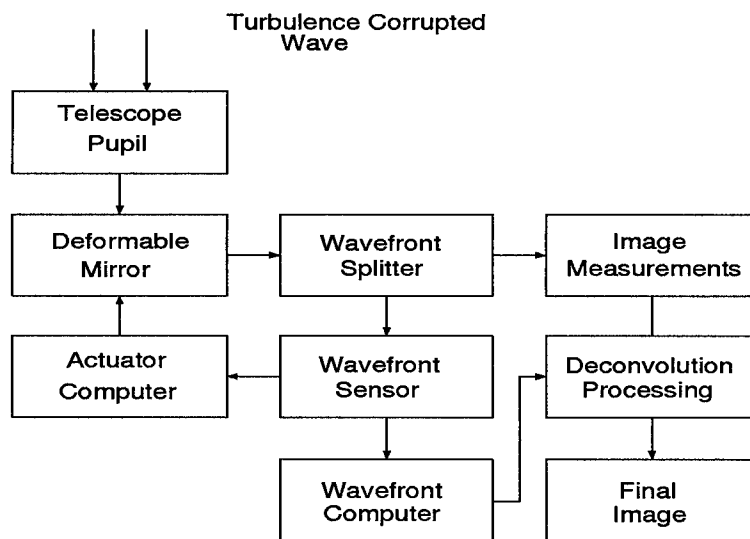


Figure 6. Functional block diagram of unfolded, open-loop adaptive-optics system modeled in the CDWFS work presented in this thesis.

cedure reads the appropriate run parameters and performs preliminary calculations used by the phase screen generator. The setup procedure also creates the appropriately scaled computer templates for the pupil and the wavefront sensor (WFS) and computes the positions of the actuators in the pupil of the telescope.

All the adaptive optics components are assumed to have the telescope pupil perfectly imaged on them, and thus locations of WFS subapertures and deformable-mirror (DM) actuators are computed in the pupil of the telescope. A 1-meter diam-

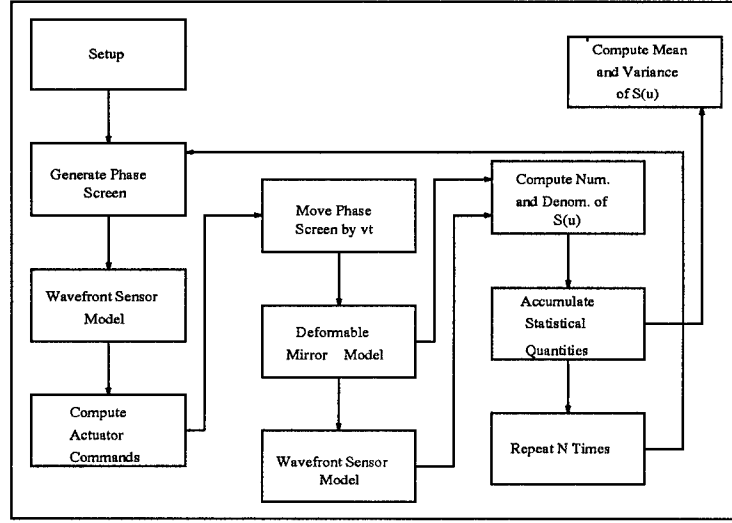


Figure 7. Block diagram for simulation; \vec{vt} is defined in the text.

eter unobscured telescope is used as the telescope model. The wavefront sensor has 12 Hartmann-type subapertures across the diameter of the telescope, for a total of 88 subapertures in the pupil. The deformable mirror has user-selectable separation between actuators placed on a Cartesian grid. For the results presented here the actuators are placed 12 cm apart in the pupil of the telescope, for a total of 57 actuators. Figure 8 shows the geometrical layout of the subapertures and the actuators, where d is the length of the subaperture. Atmospheric coherence lengths, r_o , of 7 and 10 cm are used in the calculations.

The effects of atmospheric turbulence are modeled by the presence of a thin phase screen in the pupil of the telescope. The phase screens are generated with a technique known to provide statistics that possess the phase structure function for Kolmogorov turbulence, $D_\phi(\rho)$,

$$D_\phi(\rho) = 6.88 \left(\frac{\rho}{r_o} \right)^{5/3}. \quad (15)$$

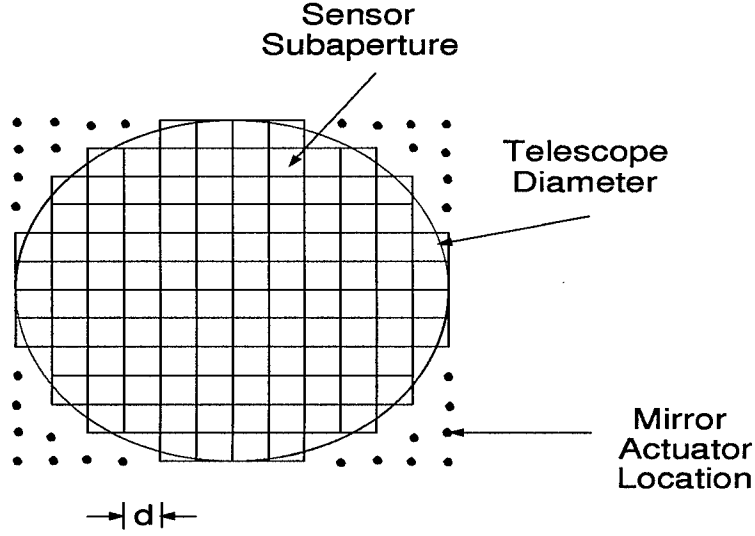


Figure 8. Wavefront sensor and mirror actuator geometry

The effects of scintillation are ignored in the simulation, though these effects can be significant for strong turbulence. Full-aperture tilt is perfectly removed from the raw turbulence-corrupted wavefront for all results shown here.

A Hartmann sensor with square subapertures is used as the wavefront sensor. The model for the Hartmann sensor measurements is given in [22] and [24]. The Hartmann sensor model used here computes a vector of noise-free slopes from the input phase screen. A Gaussian random variable of appropriate variance is then added to the noise-free slope measurements to simulate the effects of measurement noise. The standard deviation, σ_n , of this random variable is determined by the user-specified average number of photoevents per subaperture per integration time, the size of the subaperture, and the atmospheric coherence diameter and is given by [24]

$$\sigma_n = \begin{cases} \sqrt{\frac{0.86\pi\eta}{\sqrt{K_W}r_o}} & L > r_o \\ \sqrt{\frac{0.74\pi\eta}{\sqrt{K_W}L}} & L \leq r_o, \end{cases} \quad (16)$$

where L is the length of one side of a subaperture, η is an efficiency factor with typical value $\eta = 1.5$ used here, and K_W is the average number of photoevents

per subaperture per integration time. One specifies the locations of the Hartmann subapertures by providing the number of subapertures to be placed across the pupil of the telescope. The subapertures are placed on a Cartesian grid and the pupil is superimposed. All subapertures that have any portion of their area outside the pupil are removed. For all the results shown here, the number of samples across one side of a subaperture is fixed at five.

Actuator commands are computed with the least-squares, or closed-loop reconstructor [17, 22]. A vector-matrix multiplication maps the Hartmann sensor measurements to the actuator command vector for the deformable mirror. The deformable mirror model is a continuous face sheet mirror with actuators on a Cartesian grid. Influence functions are Gaussian shaped [15, 24], with the $1/e$ distance set equal to the spacing between actuators. The figure of the deformable mirror, $\phi_{DM}(x)$, is the sum of the product of actuator commands and the actuator-influence function,

$$\phi_{DM}(x) = \sum_{j=1}^J c_j e_j(x), \quad (17)$$

where c_j is the j th entry in the actuator command vector, $e_j(x)$ is the influence function of the j th actuator, and the summation is taken over the J actuators. The residual wavefront error $\phi_\epsilon(x)$ is the difference between the incident wavefront phase and the figure of the deformable mirror. The residual wavefront error is used to compute the instantaneous OTF, $H(u)$, with standard Fourier methods [5].

Deformable-mirror dynamics are neglected in the simulation. However, the effect of the delays are accounted for between sensing and correcting for a given realization of the turbulence-corrupted phase screen by shifting the phase screen along by $\vec{v}t$, where \vec{v} is the mean velocity of the phase perturbations in the pupil of the telescope and t is the time delay between wavefront sensing and correction. Taylor's frozen-field hypothesis [6] is adopted in this work. This hypothesis is implemented in the simulation by sensing the wavefront with the first WFS, shown in Figure 6, and

computing an actuator command vector. The phase screen is then translated by $\vec{v}t$ and subtracted from the deformable-mirror figure. Unsensed and uncorrected phases are shifted into the pupil of the telescope by the phase screen translation operation before the implementation of the deformable mirror correction. The resulting phase error is then passed to the second WFS in the unfolded model of the closed-loop system, shown in Figure 6.

The second wavefront sensor has a geometry identical to the first wavefront sensor but has as its input the residual wavefront phase error. The estimate of the residual wavefront, $\tilde{\phi}_\epsilon(x)$, is also computed with the least-squares reconstructor [17, 22] using Gaussian elementary fitting functions. However, a denser array of elementary functions is used to estimate residual phase. Specifically, the Gaussian elementary functions used to compute $\tilde{\phi}_\epsilon(x)$ were placed on a Cartesian grid with a 10-cm spacing and a $1/e$ width equal to 10 cm. The residual phase, $\tilde{\phi}_\epsilon(x)$, is then used to calculate the estimated instantaneous OTF, $\tilde{H}(u)$, by means of standard Fourier methods [5]. The estimated instantaneous OTF and the actual estimated OTF are then used to compute a single realization of the CDWFS transfer function, $S(u)$. Quantities required for computation of the mean and variance of the numerator and denominator of $S(u)$ and the mean and variance of the compensated OTF $H(u)$ are accumulated over a user-specified ensemble of N phase screens and stored. The results reported in [14] are for runs with $N = 200$.

3.2.2 Extended Object Imaging. Modifications are made to the simulation code used by Roggemann and Meinhardt [14] to allow an investigation of imaging extended objects. Specifically, portions of the imaging package HYSIM are incorporated into the previous simulation code and modified to perform extended object imaging. In the setup of the simulation, an object is read into the program and scaled for the proper range, wavelength, telescope diameter, and the OTF radius. The Fourier transform of the object is calculated and normalized. In the main loop of the simulation, the image spectrum is calculated from the familiar image spec-

trum expression, $I(u) = O(u)H(u)$, where $H(u)$ is the actual instantaneous OTF. The image is calculated by taking the inverse Fourier transform of the image spectrum. From the normalized image and the average number of photoevents per pixel, the Poisson image is constructed. This image is Fourier transformed to obtain the photon-limited image spectrum. The CDWFS image spectrum is calculated from

$$I^{CDWFS}(u, v) = I(u, v) \frac{\tilde{H}^*(u, v)}{|\tilde{H}(u, v)|}, \quad (18)$$

$$I^{CDWFS}(u, v) = O(u, v)H(u, v) \frac{\tilde{H}^*(u, v)}{|\tilde{H}(u, v)|}, \quad (19)$$

where I^{CDWFS} is the instantaneous CDWFS image spectrum, $I(u, v)$ is the instantaneous image spectrum, and $\tilde{H}(u, v)$ is the estimated instantaneous OTF. The CDWFS image spectrum is averaged over the N frames of data, where $N = 200$ for the results presented here. The CDWFS image is calculated by inverse Fourier transforming the average CDWFS image spectrum.

3.2.3 Performance Metric. In order to properly interpret the improvement in optical performance due to the CDWFS technique, the CDWFS technique is compared to the conventional method of deconvolution. The metric used to compare the deconvolution image and the CDWFS image is the mean-square Fourier phase error between the actual object spectrum and each of the estimated image spectra. This is accomplished through the use of

$$I_{OBJ}(u, v) = |I_{OBJ}(u, v)|e^{j\phi_{OBJ}(u, v)}, \quad (20)$$

where $|I_{OBJ}|$ is the magnitude of the actual object spectrum and ϕ_{OBJ} is the phase of the actual object spectrum. For each of the two image reconstruction approaches,

CDWFS and deconvolution, an estimated image spectrum is calculated

$$\tilde{I}(u, v) = |\tilde{I}(u, v)|e^{j\tilde{\phi}(u, v)}, \quad (21)$$

where $|\tilde{I}|$ is the magnitude of the estimated image spectrum and $\tilde{\phi}$ is the phase of the estimated image spectrum. The mean-square Fourier phase error is calculated for both the CDWFS and the deconvolution image spectrums using

$$|I_{OBJ}(u, v)|e^{j\phi_{OBJ}(u, v)} \times |\tilde{I}(u, v)|e^{j\tilde{\phi}(u, v)} = |I_{OBJ}(u, v)||\tilde{I}(u, v)| \exp j[\phi_{OBJ} - \tilde{\phi}] \quad (22)$$

where the phase error is determined from the exponential. Equation (23) is used to calculate the mean-square Fourier phase error.

$$\epsilon_{\phi(u, v)}^2 = \langle [\phi_{OBJ}(u, v) - \tilde{\phi}(u, v)]^2 \rangle, \quad (23)$$

where $\epsilon^2(u, v)$ is the mean-square Fourier phase error. The mean-square Fourier phase error is radially averaged for comparison purposes.

An important point that needs to be considered when calculating the mean-square Fourier phase error of the actual object spectrum and the estimated image spectrums is that each needs to be recentroided before the difference between Fourier phases is calculated. Shifts between the actual object spectrum and the estimated spectrum results in large Fourier phase errors. Recentroiding ensures that the spectrums are aligned properly before the mean-square Fourier phase errors are calculated. Matlab is used to calculate the phase of each image and these values range from $-\pi$ to $+\pi$ radians.

3.2.4 Photon Levels. An important part of good imaging includes having enough light to provide good reconstructed images. As the light levels decrease, the reconstructed images become overtaken by noise. The light levels are determined by the number of photons available for the WFS and for image reconstruction. Thus

by varying the available photons for the WFS and for image reconstruction, the simulation can demonstrate imaging of objects of varying brightness.

In the simulations performed by Roggemann and Meinhardt [14], the values for the average number of photoevents/image/integration time and the average number of photoevents/subaperture/integration time for the wavefront sensor were arbitrarily set. In the modifications made in this thesis, computer generated photon flux values are used. The program used to obtain these values was written by Terry M. Gray of the Kirtland AFB Phillips Laboratory passive imaging branch. The program calculates the photon flux detected at the ground detector based on the visual magnitude of the object being imaged. The resulting photon flux then, is a function of the visual magnitude of the object, the mean wavelength and the wavelength bandwidth. Table 1 shows the photon flux values generated by this program for the imaging photon count. The wavelength, λ_{img} , telescope transmission factor, τ , bandwidth, BW,

Visual magnitude	Photon flux (photons/s m^2)
0.0	0.6825×10^9
1.0	0.2717×10^9
2.0	0.1082×10^9
3.0	0.4306×10^8
4.0	0.1714×10^8
5.0	0.6825×10^7
6.0	0.2717×10^7
7.0	0.1082×10^7
8.0	0.4306×10^6

Table 1. Photon flux values for the image with $\lambda_{img} = 0.7\mu m$, $\tau = 0.1$, BW = 10%

and visual magnitude are input into this program and the flux values are determined from these input parameters. The values used to generate the photon flux values are shown in Table 1. K_I is the average number of photoevents/image/integration time and is calculated from

$$K_I = (\text{photon flux}) \times (\text{area of pupil}) \times (\text{integration time}), \quad (24)$$

where the area of the pupil is calculated by πr^2 , where r is the radius of the image pupil. The photon flux values are found in Table 1 and Table 2 shows the values used for the area of the pupil and the integration time.

	Area (m ²)	Integration Time (ms)
Telescope (K_I)	0.785398	10
WFS (K_W)	0.00694	3.33

Table 2. Simulation parameters used in the calculation of K_I and K_W

Table 3 shows the photon flux values generated for the wavefront sensor photon count and the values of the input parameters. K_W is the average number of photoevents/subaperture/integration time and is calculated from Equation (25),

$$K_W = (\text{photon flux}) \times (\text{area of subaperture}) \times (\text{integration time}), \quad (25)$$

where the WFS photon flux value is found in Table 3 and the area of the subaperture and integration time are found in Table 2. Table 4 shows the calculated values of K_I and K_W that are used when imaging objects of various visual magnitudes.

Visual magnitude	Photon flux (photon/ s m^2)
0.0	0.1365×10^{10}
1.0	0.5434×10^9
2.0	0.2163×10^9
3.0	0.8613×10^8
4.0	0.3429×10^8
5.0	0.1365×10^8
6.0	0.5434×10^7
7.0	0.2163×10^7
8.0	0.8613×10^6

Table 3. Photon flux values for the WFS with $\lambda_{img} = 0.6\mu m$, $\tau = 0.1$, BW = 20%

Visual Magnitude	K_I	K_W
	average number of	average number of
	photoevents/image/ integration time	photoevents/subaperature/ integration time
0.0	5360341	27798
1.0	2133926	11063
2.0	849800	4404
3.0	338192	1753
4.0	134617	698
5.0	53603	277
6.0	21339	110
7.0	8498	44
8.0	3381	17

Table 4. K_I and K_W calculated from photon flux values

3.3 *Conclusion*

This chapter set forth the methodology that is used to examine the CDWFS imaging technique. The first section describes the simulation used by Roggemann and Meinhardt [14]. The following section discusses the modifications made to the program in order to image extended objects with the CDWFS technique. Deconvolution is also discussed so that the CDWFS technique can be compared to the conventional post processing method. The mean-square Fourier phase error is developed in order to compare the CDWFS results and the deconvolution results. Computer generated photon values are incorporated into both simulations to simulate imaging of objects of various visual magnitudes. The results are presented in Chapter IV and the conclusions and recommendations are discussed in Chapter V.

IV. Results

4.1 Introduction

This chapter explores the feasibility of using the CDWFS technique in imaging extended objects. Chapter three developed a methodology for conducting this investigation. The simulation code used in reference [14] is modified to include imaging of extended objects, instead of star imagery that was used in previous results. The modified simulation produces an average CDWFS image. Deconvolution is simulated using HYSIM under the same conditions as the CDWFS technique. The primary parameters used to compare the CDWFS results and the deconvolution results include the time delays in the closed-loop system, the atmospheric seeing conditions and computer generated photon values. The CDWFS image and the deconvolution image are compared directly for these various parameters. This comparison is performed using the mean-square Fourier phase error, $\epsilon^2(u, v)$, of each image spectrum estimate with the actual object spectrum.

Four experiments are performed to test the primary parameters. Experiment one compares the images when the time delays ($\vec{v}t$) in the closed-loop system are 0, 5, 10 and 20 cm, where \vec{v} is the mean velocity of the phase perturbations in the pupil of the telescope and t is the time delay between sensing and correcting for a realization of the turbulence. The distances $\vec{v}t$ used above would arise, for example, in the case of 20 km/h wind (that is, the velocity of the phase across the pupil with Taylor's frozen-field hypothesis) in a system with the following closed-loop bandwidths (BW's): 0 cm, BW = ∞ ; 5 cm, BW = 111 Hz; 10 cm, BW = 55 Hz; 20 cm, BW = 28 Hz. Changing the time delay changes the bandwidth of operation. Experiment two is the same as experiment one except that the atmospheric coherence diameter, r_o , is changed from 0.10 m to 0.07 m (effectively reducing the seeing conditions). Experiment three incorporates the computer generated photon values. The visual magnitude of the object ranges from 0.0 to 8.0 and the delay time is set

to 0 cm. Experiment four sets the visual magnitude to 0.0, 5.0, 7.0 and 8.0 but increases the delay time, \vec{vt} , to 10 cm.

For each experimental result, an average CDWFS image and a deconvolution image are presented for comparison of both approaches. The phase spectrum estimation accuracy is obtained by computing the square of the difference between the actual object phase spectrum and the estimated image phase spectrum at every point in a sampled frequency space and then radially averaging to obtain a plot of the mean-square phase spectrum error as a function of the spatial frequency magnitude. The normalized spatial frequency at which the radially averaged mean-square Fourier phase error becomes greater than 0.3 rad^2 , referred to as f_{eff} , is a useful if somewhat arbitrary metric for determining the spatial frequency cutoff of the Fourier phase spectrum estimate.

4.1.1 System Parameters. Common optical system parameters are used for all simulations. The simulated system is a 1 meter unobscured adaptive optics telescope. The imaging wavelength is 700 nm, with a 10% fractional bandwidth, and the wavefront sensor wavelength is 600 nm, with a 20% fractional bandwidth. The image sets generated by the simulation consist of 200 frames. The image photon flux values are calculated based on a telescope transmission factor of 0.10, the wavelengths given above, the bandwidths given above, and the visual magnitudes ranging from 0.0 to 8.0. The wavefront sensor is assumed to operate at a sampling rate of 3.3 ms. The object used in the simulation is an Ocean Recon space satellite, and is depicted in Figure 9. The object array is assumed to be approximately 18 meters in length and orbiting at a distance of approximately 600 kilometers.

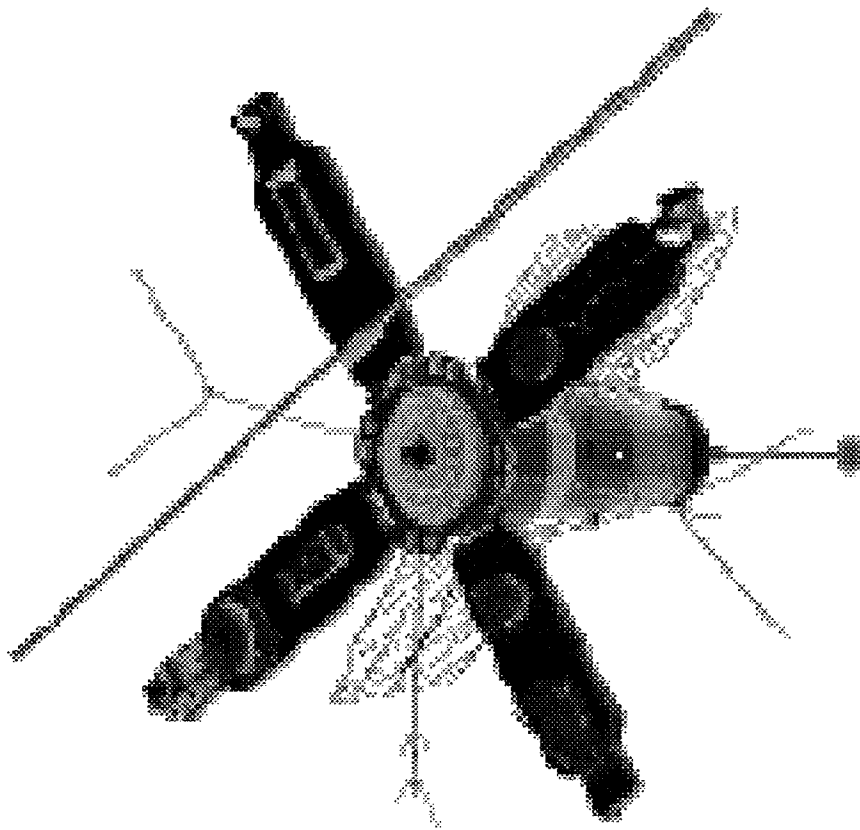


Figure 9. Typical Space Satellite

4.2 Experiment one

This experiment is the initial investigation into the implementation of the CDWFS technique in imaging extended objects. The performance of the CDWFS technique and the deconvolution technique are compared for various delay times.

4.2.1 Simulation Parameters. The object's visual magnitude, m_ν , is set to 0.0. The parameter r_o is set to 10 cm to simulate 'average' seeing conditions at a good observatory. The resulting K_I and K_W for m_ν equal to 0.0 can be found in Table 4. The delay time, \vec{vt} , is varied from 0, 5, 10 and 20 cm, effectively decreasing the closed-loop bandwidth, as \vec{vt} increases.

4.2.2 Simulation Results. This experiment investigates the use of the CDWFS technique when the time delays are varied in the closed-loop system. Figure 10 shows the results when the delay time, \vec{vt} , is set to an ideal 0 cm. Applying the Fourier phase error metric to this case, yields an $f_{eff} = 99\%$ for the CDWFS image and $f_{eff} = 93\%$ for the deconvolution image. Figure 11 shows the results when the time delay is increased to 5 cm. For the CDWFS image, $f_{eff} = 89\%$, while the deconvolution image has $f_{eff} = 80\%$. With a delay of 10 cm, the CDWFS image in Figure 12 has an $f_{eff} = 90\%$ while the deconvolution image $f_{eff} = 50\%$. At a delay of 20 cm, the CDWFS image has an $f_{eff} = 92\%$ and the deconvolution $f_{eff} = 28\%$. Figure 14 depicts all four of the CDWFS radially averaged mean-square Fourier phase error curves (top) and all four of the deconvolution Fourier phase error curves (bottom). From these results, the CDWFS technique performs better over the range of time delays when the mean-square Fourier phase error is used as the performance metric.

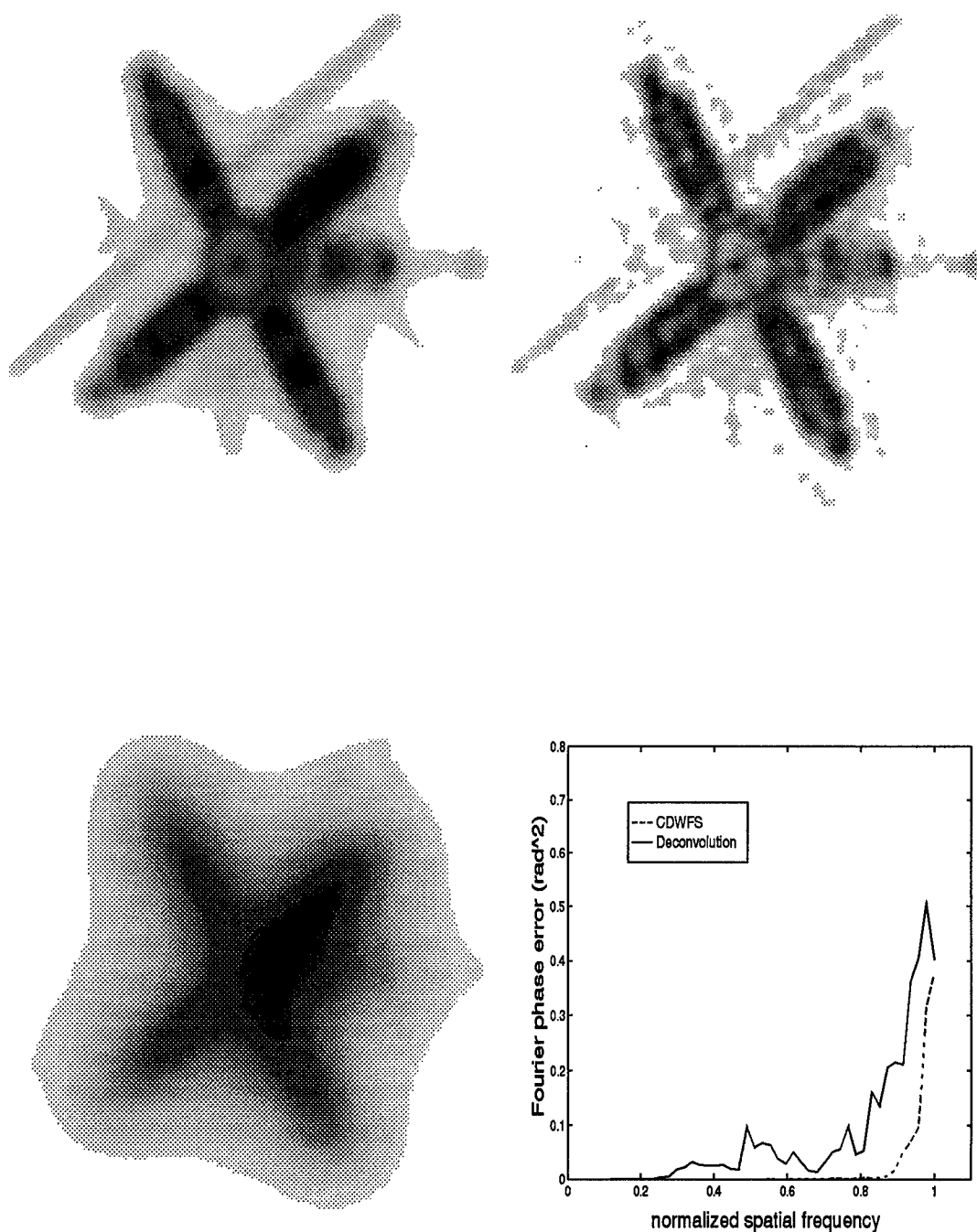


Figure 10. Average CDWFS image (top left), average deconvolved image (top right), long exposure image (bottom left) and the radially averaged mean-square Fourier phase error (bottom right) with a delay time, vt , of 0 cm

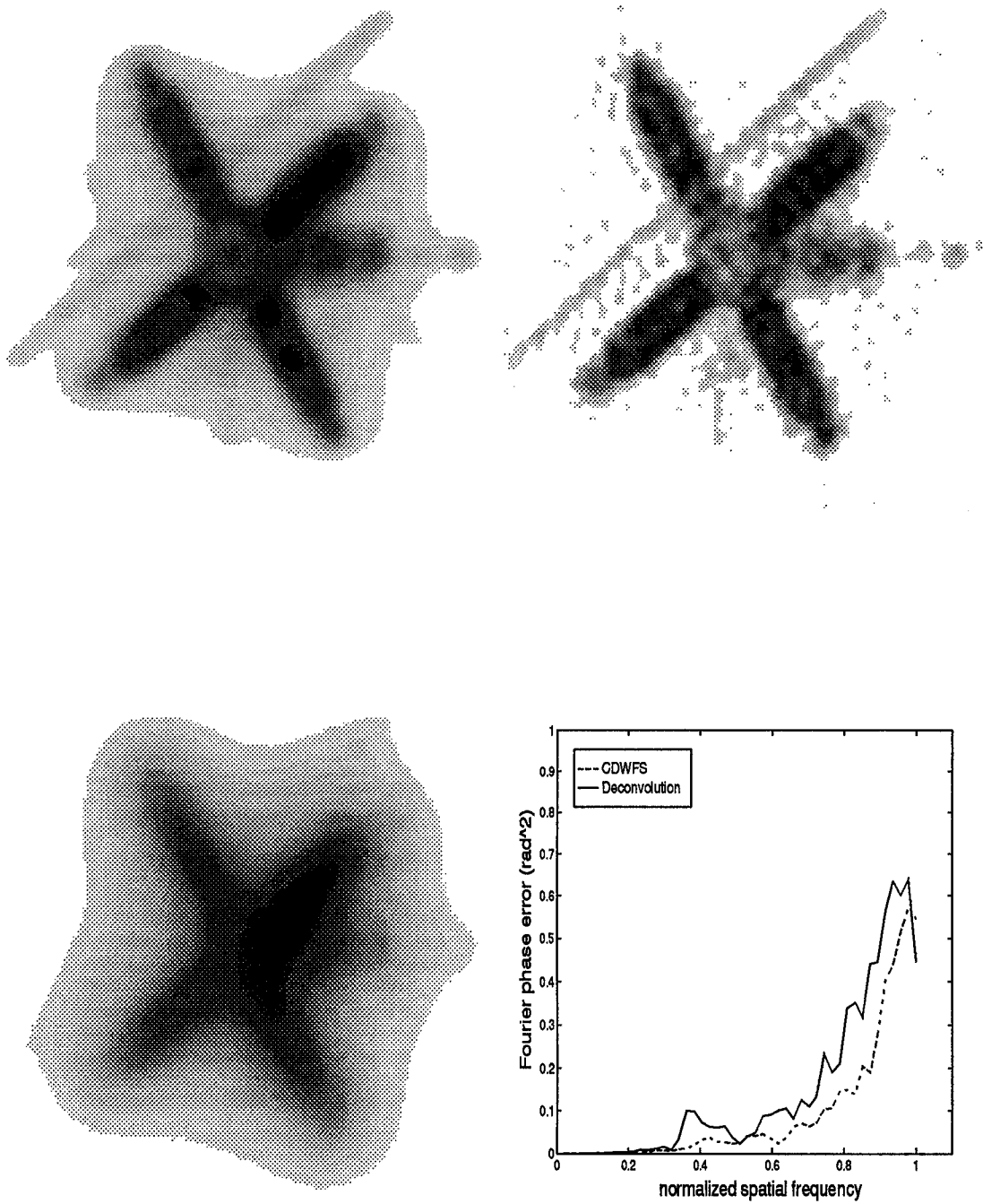


Figure 11. Average CDWFS image (top left), average deconvolved image (top right), long exposure image (bottom left), and the radially averaged mean-square Fourier phase error (bottom right) with a delay time, vt , of 5 cm

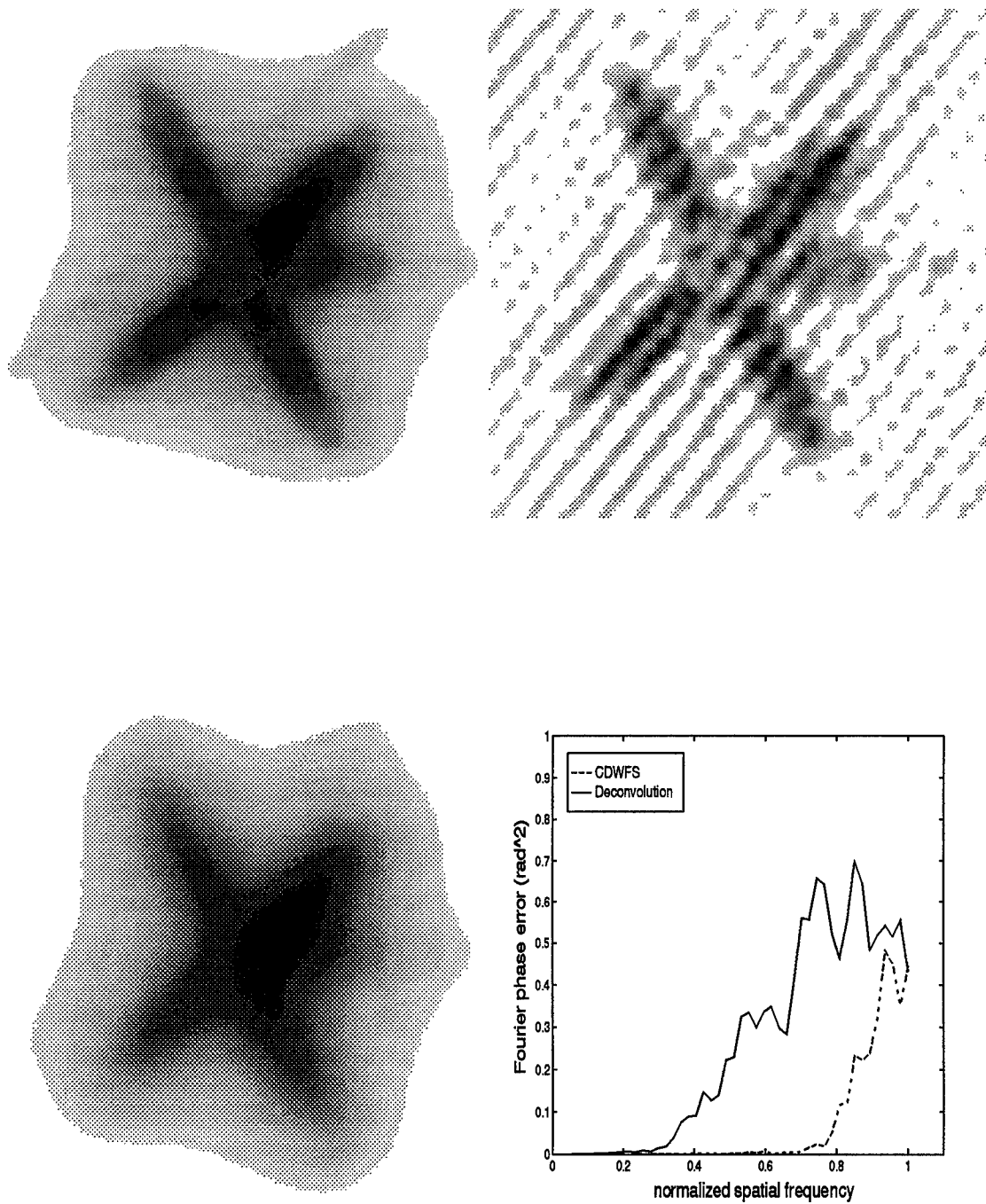


Figure 12. Average CDWFS image (top left), average deconvolved image (top right), long exposure image (bottom left), and the radially averaged mean-square Fourier phase (bottom right) error with a delay time, vt , of 10 cm

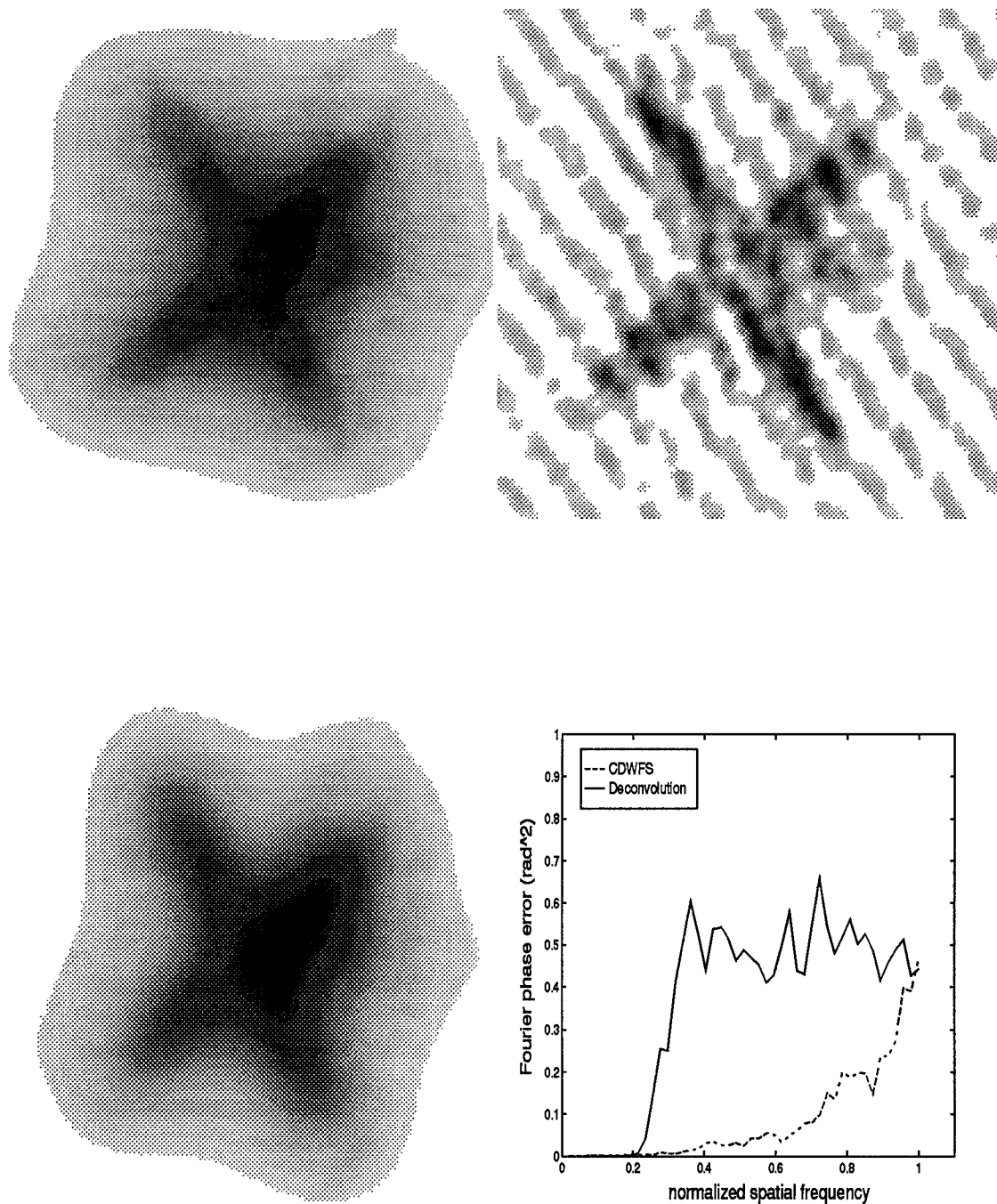


Figure 13. Average CDWFS image (top left), average deconvolved image (top right), long exposure image (bottom left), and the radially averaged mean-square Fourier phase error (bottom right) with a delay time, vt , of 20 cm

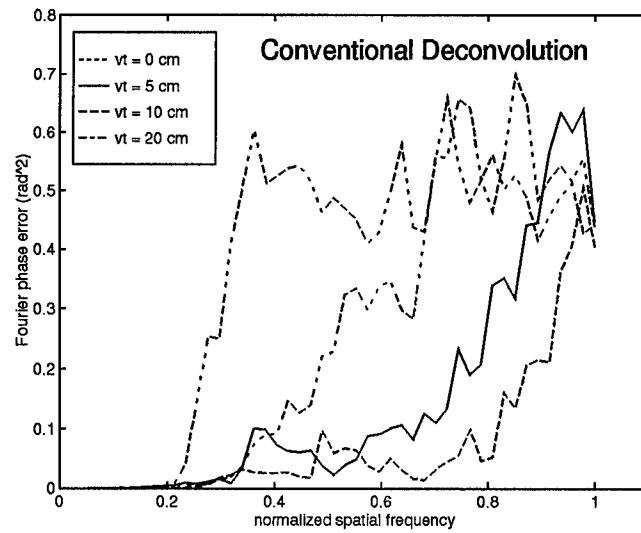
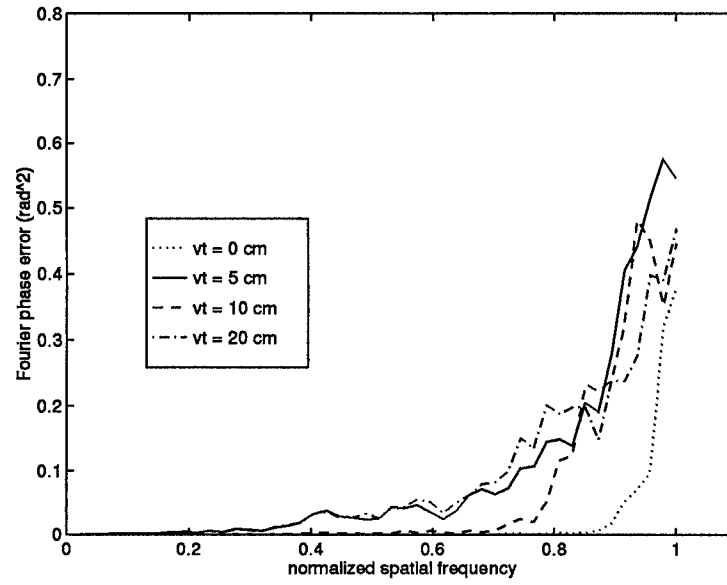


Figure 14. Radially averaged mean-square Fourier phase errors for the average CD-WFS images (top) and the deconvolution images (bottom) with delay time of 0 cm, 5 cm, 10 cm and 20 cm

4.2.3 Conclusion. This experiment demonstrates the effect of increasing the time delay in the closed-loop system. As the delay increases from 0 cm to 20 cm, the CDWFS Fourier phase error effective cutoff only increases at most 10%, while the deconvolution Fourier phase error effective cutoff increases by at most 65%. The CDWFS technique allows longer delay times in the closed-loop system while providing reconstructed images without introducing considerably more Fourier phase errors. The use of longer delay times implies that the bandwidth of operation can be reduced. This reduction of the closed-loop bandwidth permits longer integration times in the WFS, which then allows dimmer objects to be imaged without the use of an artificial guidestar.

4.3 Experiment two

This experiment investigates the performance of the CDWFS technique with respect to ‘poor’ seeing conditions. The performance of the CDWFS technique and the deconvolution technique are compared for various time delays.

4.3.1 Simulation Parameters. The object’s visual magnitude, m_ν , is set to 0.0. The resulting K_I and K_W for m_ν equal to 0.0 can be found in Table 4. The parameter r_o is set to 7 cm to simulate “poor” seeing conditions. The delay time, \vec{vt} , is varied from 0, 5, 10, and 20 cm, effectively decreasing the closed-loop bandwidth, as \vec{vt} increases.

4.3.2 Simulation Results. This experiment investigates the use of the CDWFS technique when the seeing conditions are ‘poor’. Figure 15 shows the results for a delay time of an ideal 0 cm. The CDWFS Fourier phase error yields an $f_{eff} = 93\%$ and the deconvolution Fourier phase error yields an $f_{eff} = 30\%$. Figure 16 provides the results for a delay of 5 cm. The CDWFS Fourier phase error effective cutoff, f_{eff} , is equal to 85%, while the deconvolution Fourier phase error yields an $f_{eff} = 30\%$. For a delay of 10 cm, Figure 17 depicts the results. The CDWFS Fourier phase error yields an $f_{eff} = 80\%$ and the deconvolution Fourier phase error provides and $f_{eff} = 25\%$. Figure 18 shows the results for a delay of 20 cm. The CDWFS Fourier phase error yields $f_{eff} = 78\%$ and the deconvolution Fourier phase error yields an $f_{eff} = 20\%$. Figure 19 depicts all four CDWFS Fourier phase plots (top) and all four deconvolution Fourier phase plots (bottom). As the delay increases from 0 cm to 20 cm, the CDWFS Fourier phase error at the worst case yields an $f_{eff} = 78\%$, but the deconvolution Fourier phase error at the best case yields an $f_{eff} = 30\%$. Clearly the CDWFS technique performs better than the deconvolution technique at ‘poor’ seeing conditions for all of the four delay times simulated here.

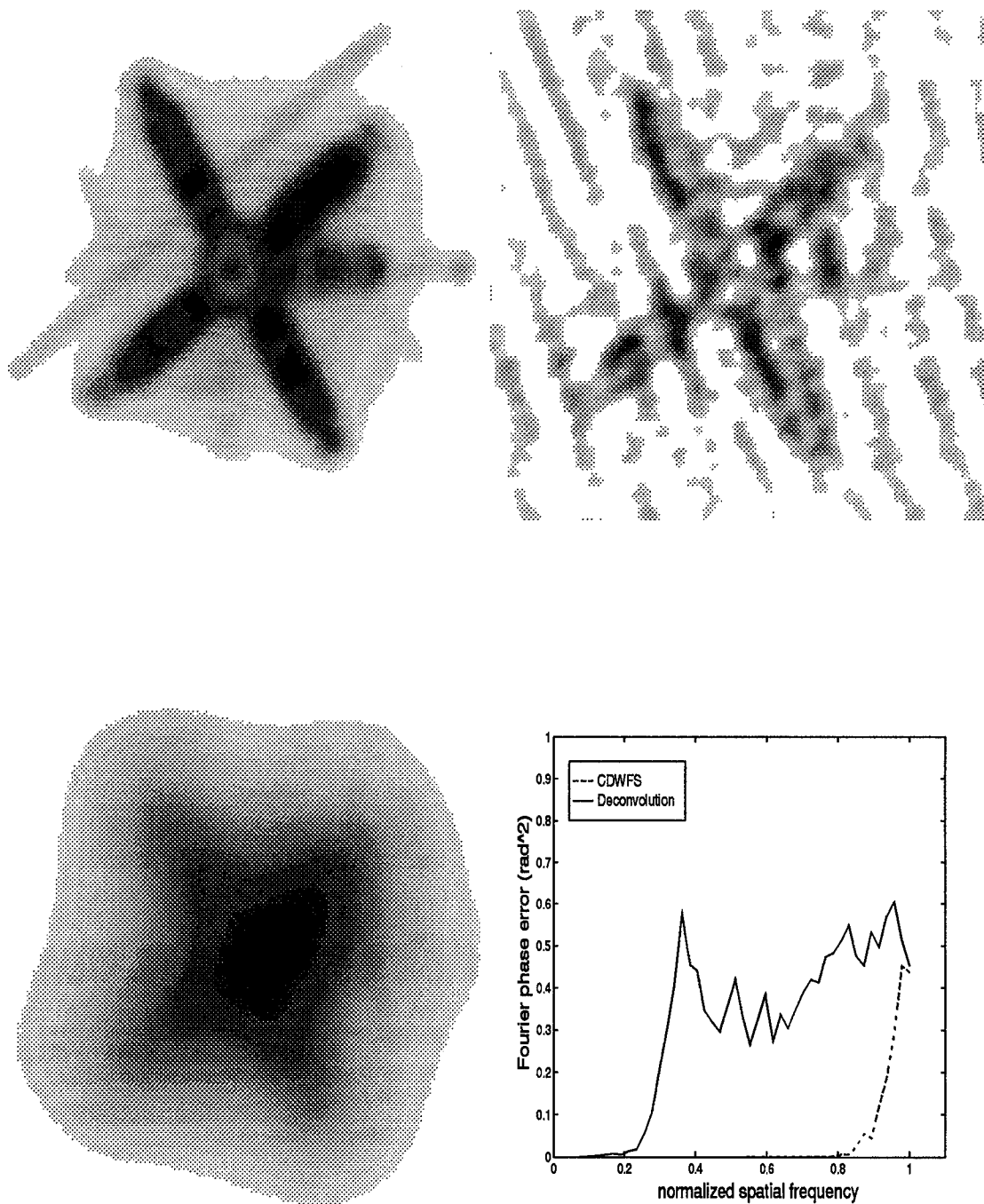


Figure 15. Average CDWFS image (top left), average deconvolved image (top right), long exposure image (bottom left), and the radially averaged mean-square Fourier phase error (bottom right) with a delay time, vt , of 0 cm

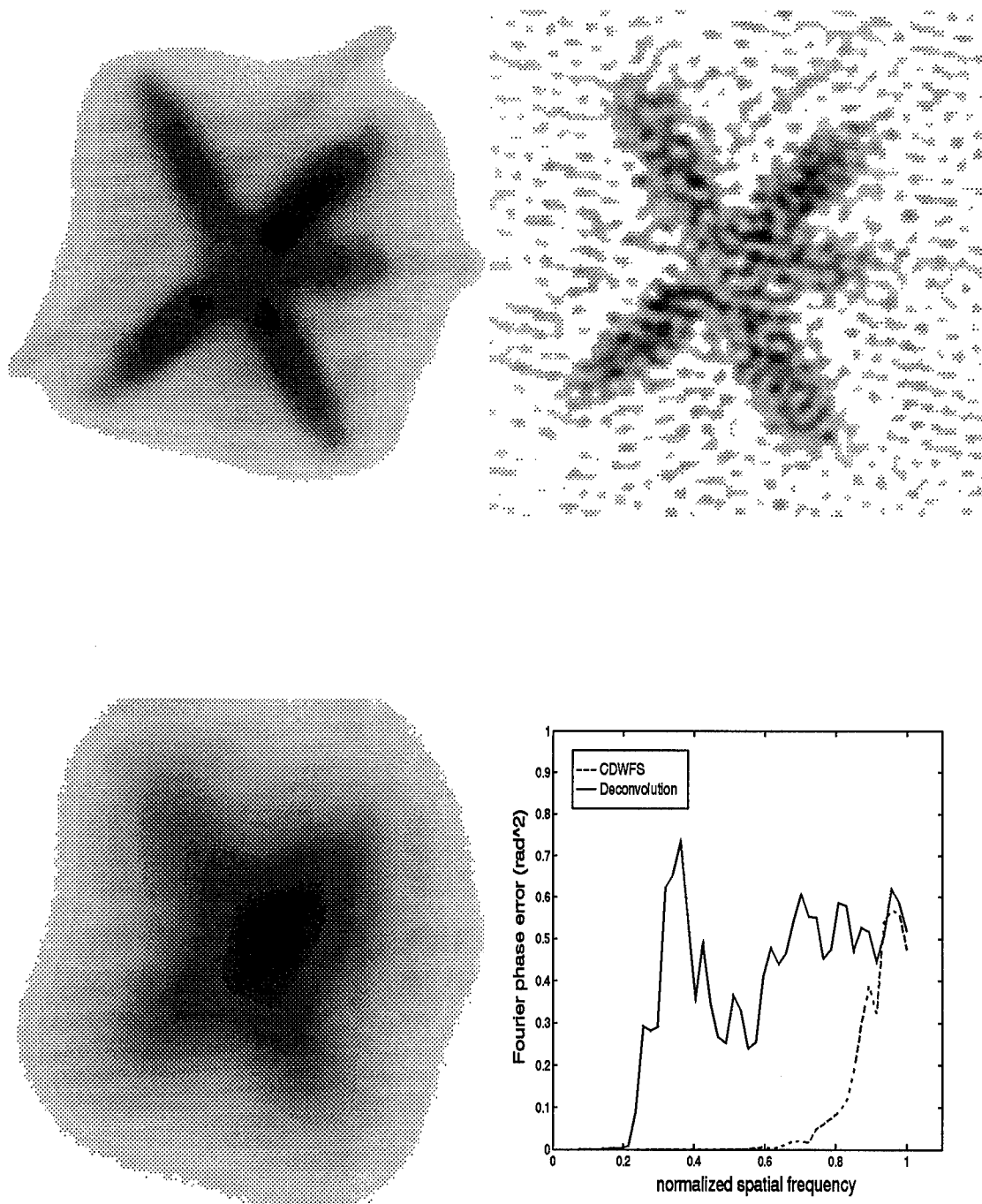


Figure 16. Average CDWFS image (top left), average deconvolved image (top right), long exposure image (bottom left), and the radially averaged mean-square Fourier phase error (bottom right) with a delay time, vt , of 5 cm

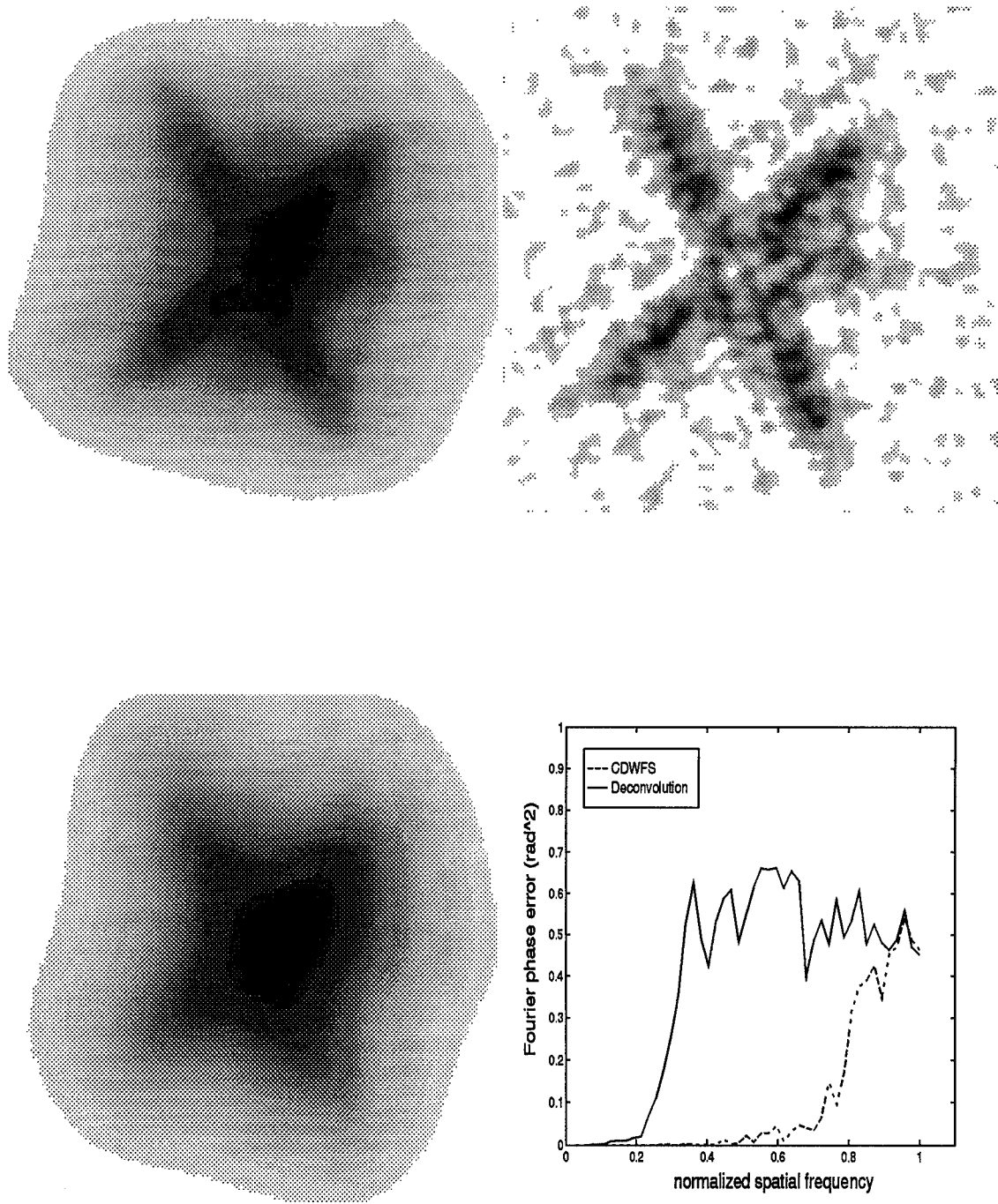


Figure 17. Average CDWFS image (top left), average deconvolved image (top right), long exposure image (bottom left), and the radially averaged mean-square Fourier phase error (bottom right) with a delay time, $\vec{v}t$, of 10 cm

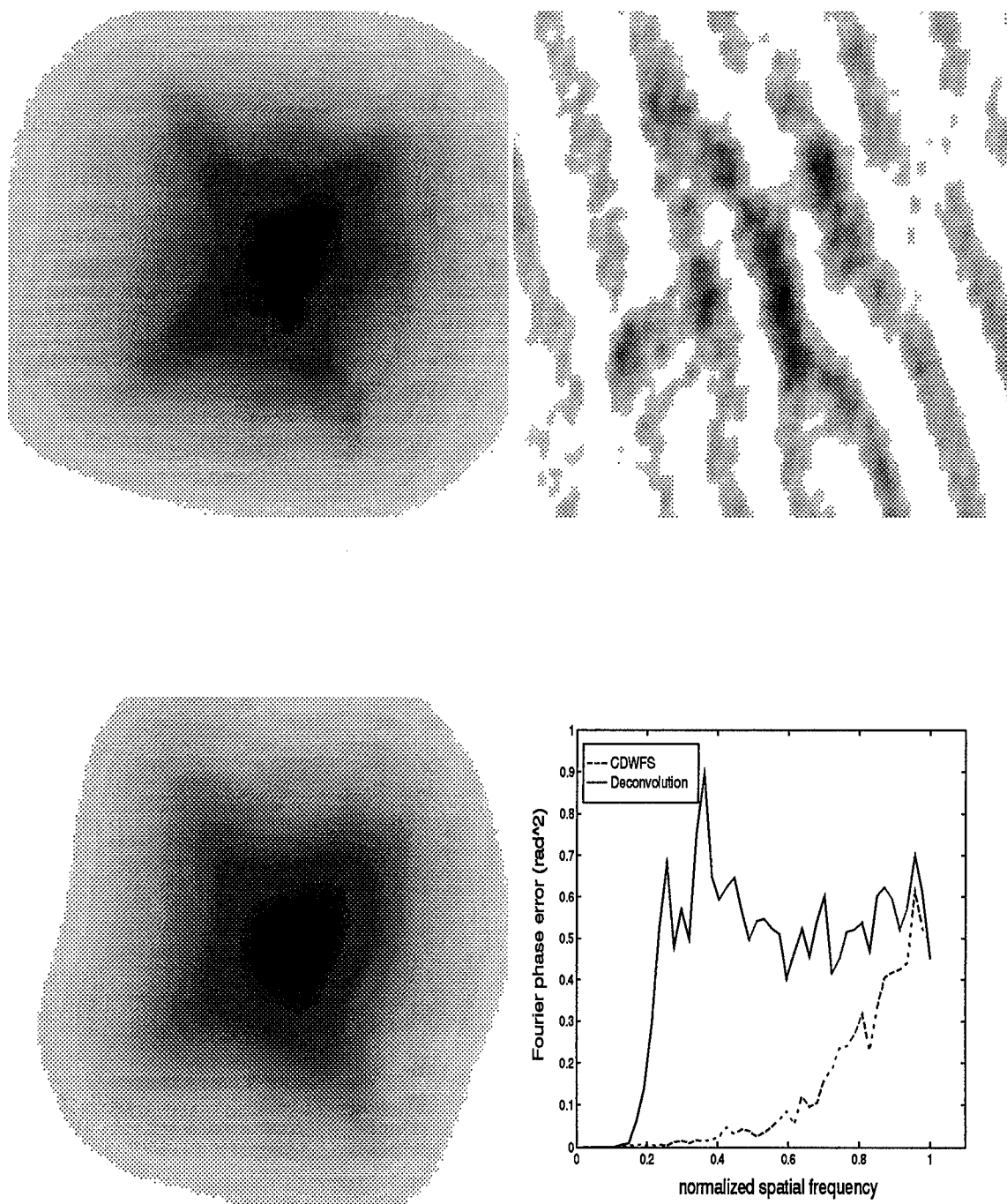


Figure 18. Average CDWFS image (top left), average deconvolved image (top right), long exposure image (bottom left), and the radially averaged mean-square Fourier phase error (bottom right) with a delay time, vt , of 20 cm

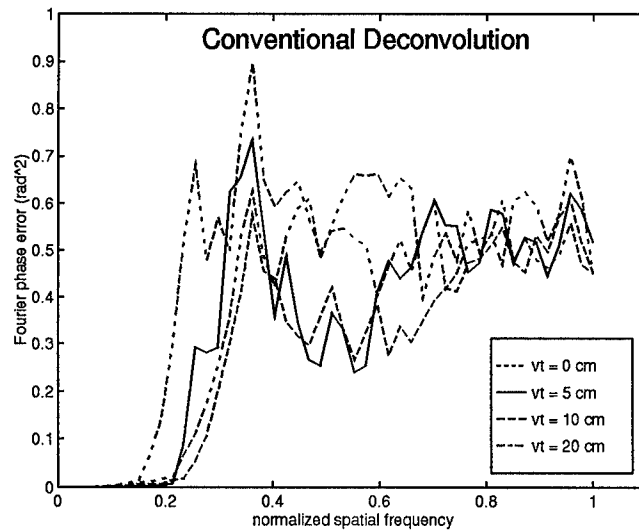
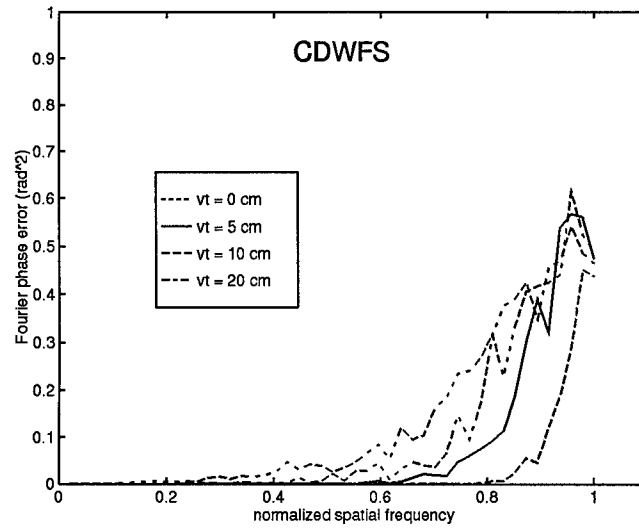


Figure 19. Radially averaged mean-square Fourier phase errors for the average CD-WFS images (top) and the deconvolution images (bottom) with delay time of 0 cm, 5 cm, 10 cm and 20 cm

4.3.3 Conclusion. This experiment demonstrates the effect of imaging under ‘poor’ seeing conditions. As the delay increase from 0 cm to 20 cm, the CDWFS Fourier phase error in the worst case yields $f_{eff} = 78\%$, while the deconvolution Fourier phase error in its best case yields $f_{eff} = 30\%$. Reducing the seeing conditions has little effect on the CDWFS technique, as can be seen from comparing Figure 14 (top) and 19 (top). The CDWFS Fourier phase error effective cutoff decreases at most by 14% when seeing conditions are changed from ‘average’ to ‘poor’. The deconvolution Fourier phase error effective cutoff decreases at most by 73%. The deconvolution technique generates images with high Fourier phase errors at all time delays. The CDWFS technique outperforms deconvolution because the ‘poor’ seeing conditions have only a slight effect on the CDWFS Fourier phase errors.

4.4 Experiment three

This experiment investigates the performance of the CDWFS technique with respect to the visual magnitude of the object of interest. The performance of the CDWFS technique and the deconvolution technique are compared for various visual magnitudes of the object with the ideal time delay of 0 cm.

4.4.1 Simulation Parameters. The parameter r_o was set to 10 cm to simulate ‘average’ seeing conditions. The delay time was set to an ideal 0 cm. The visual magnitude, m_ν , is varied from 0.0 to 8.0. The resulting K_I and K_W for these magnitudes can be found in Table 4.

4.4.2 Simulation Results. This experiment investigates the use of computer generated photon values in simulating the effect of imaging objects of various magnitudes. For a m_ν of 0.0, Figure 21 presents the results. The CDWFS Fourier phase error yields $f_{eff} = 95\%$ while the deconvolution Fourier phase error yields $f_{eff} = 90\%$. As the visual magnitude increases to 1.0, as in Figure 22, the CDWFS Fourier phase error remains at $f_{eff} = 95\%$ and the deconvolution Fourier phase error remains at $f_{eff} = 90\%$. When the visual magnitude is 2.0, as in Figure 23, the effect of limited photons begins to surface in the deconvolution results. The CDWFS Fourier phase error yields $f_{eff} = 93\%$ while the deconvolution Fourier phase error yields $f_{eff} = 80\%$. At a visual magnitude of 3.0, as in Figure 24, the CDWFS Fourier phase error and the deconvolution Fourier phase error effective cutoffs remain the same as in the case of $m_\nu = 2.0$. The magnitude of the Fourier phase errors increases, but the CDWFS Fourier phase error does not increase as much as the deconvolution Fourier phase error. In Figure 25 the visual magnitude is increased to 4.0. The CDWFS Fourier phase error yields $f_{eff} = 90\%$ while the deconvolution Fourier phase error yields $f_{eff} = 62\%$. In Figure 26 the visual magnitude is increased to 5.0. The CDWFS Fourier phase error yields $f_{eff} = 90\%$ and the deconvolution Fourier phase error yields $f_{eff} = 42\%$. Figure 27 shows the results for a visual magnitude of 6.0.

The CDWFS Fourier phase error yields $f_{eff} = 85\%$ and the deconvolution Fourier phase error yields $f_{eff} = 43\%$. Figure 28 shows the results for a visual magnitude of 7.0. The effect of the limited number of photons available is beginning to have an effect on the results of the CDWFS technique, as can be seen in the CDWFS reconstructed image. The CDWFS effective cutoff, f_{eff} , equal to 82%, while the effective cutoff of deconvolution is equal to 40%. For a visual magnitude of 8.0, Figure 28 shows the results. The CDWFS technique yields an $f_{eff} = 82\%$ and the deconvolution effective cutoff equals 30%. The limited number of photons available for reconstruction has its effect on both techniques, however, the CDWFS technique clearly outperforms the deconvolution technique based on the mean-square Fourier phase error metric, as can be seen in the reconstruction images.

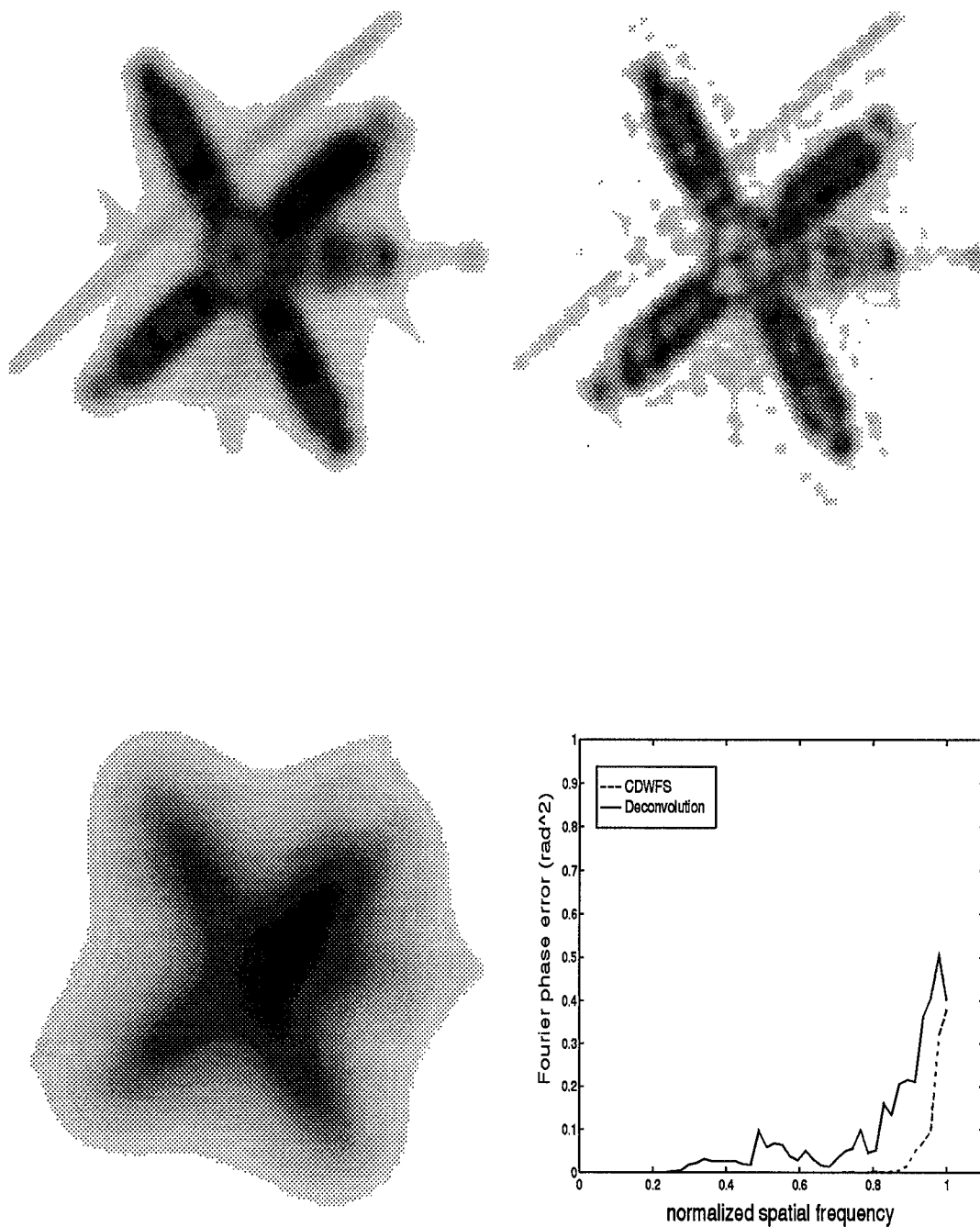


Figure 20. Average CDWFS image (top left), average deconvolved image (top right), long exposure image (bottom left), and the radially averaged mean-square Fourier phase error (bottom right) with a visual magnitude, m_ν , of 0.0 and $vt = 0$ cm

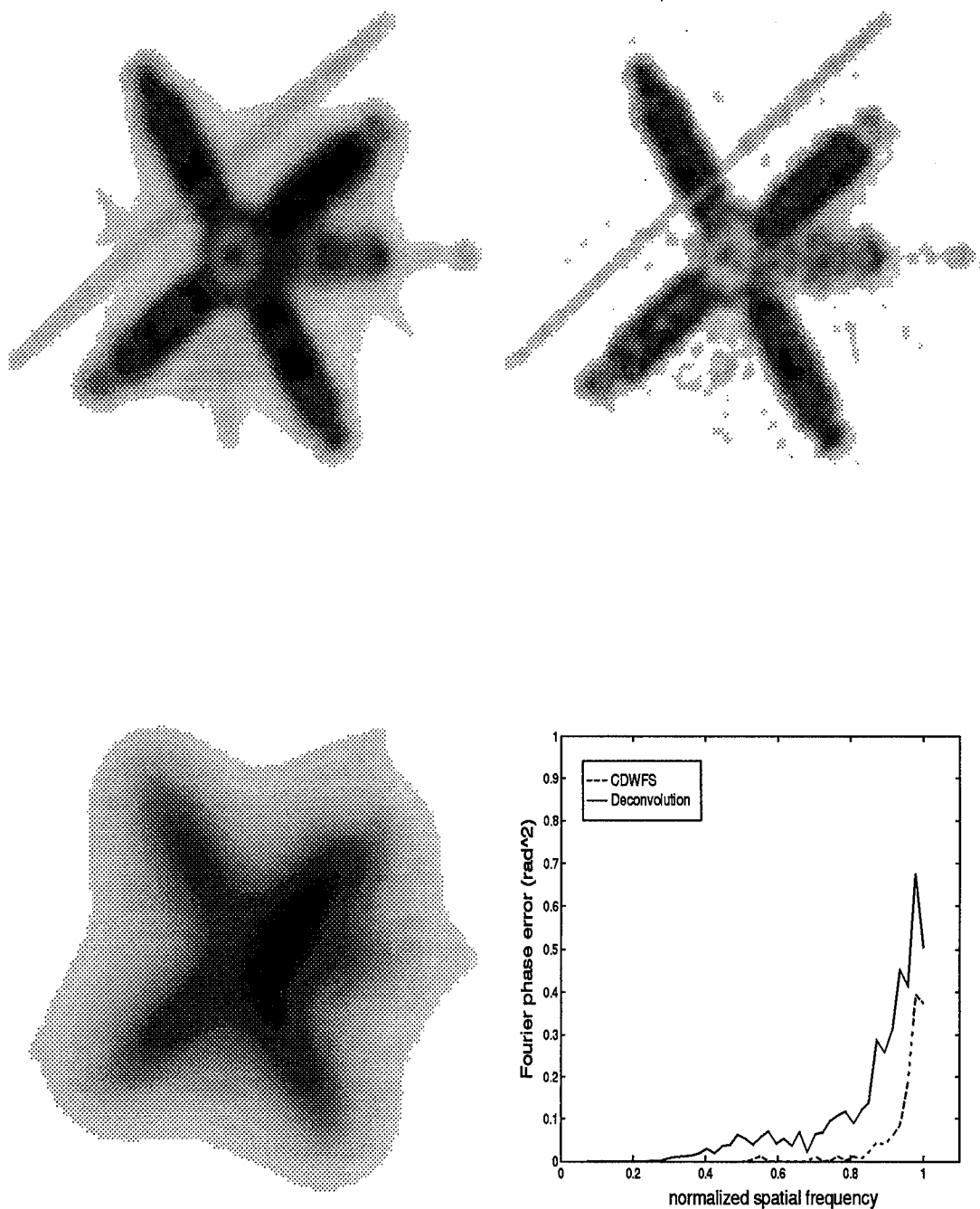


Figure 21. Average CDWFS image (top left), average deconvolved image (top right), long exposure image (bottom left), and the radially averaged mean-square Fourier phase error (bottom right) with a visual magnitude, m_v , of 1.0 and $v\bar{t} = 0$ cm

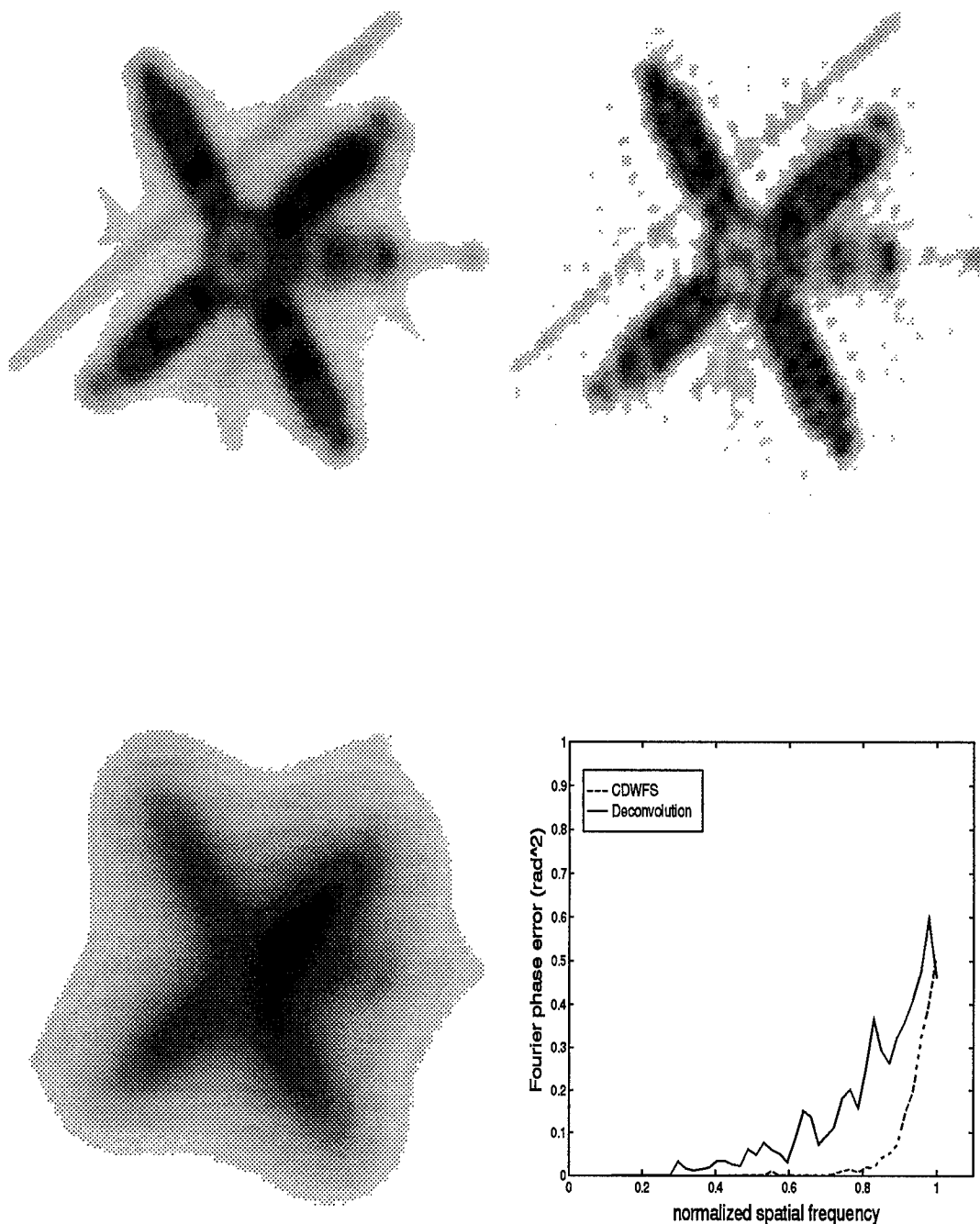


Figure 22. Average CDWFS image (top left), average deconvolved image (top right), long exposure image (bottom left), and the radially averaged mean-square Fourier phase error (bottom right) with a visual magnitude, m_v , of 2.0 and $\vec{vt} = 0$ cm

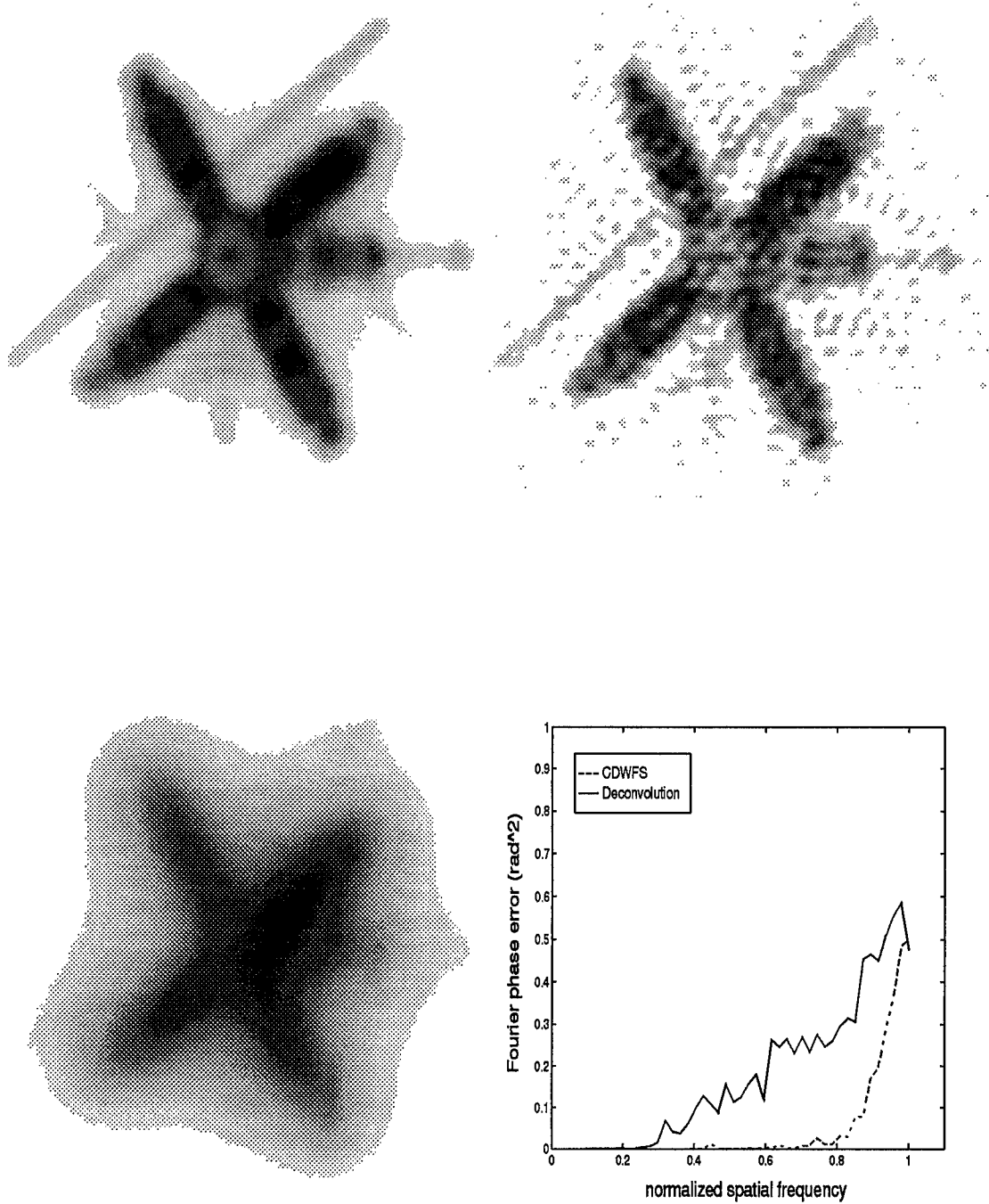


Figure 23. Average CDWFS image (top left), average deconvolved image (top right), long exposure image (bottom left), and the radially average mean-square Fourier phase error (bottom right) with a visual magnitude, m_ν , of 3.0 and $\vec{vt} = 0$ cm

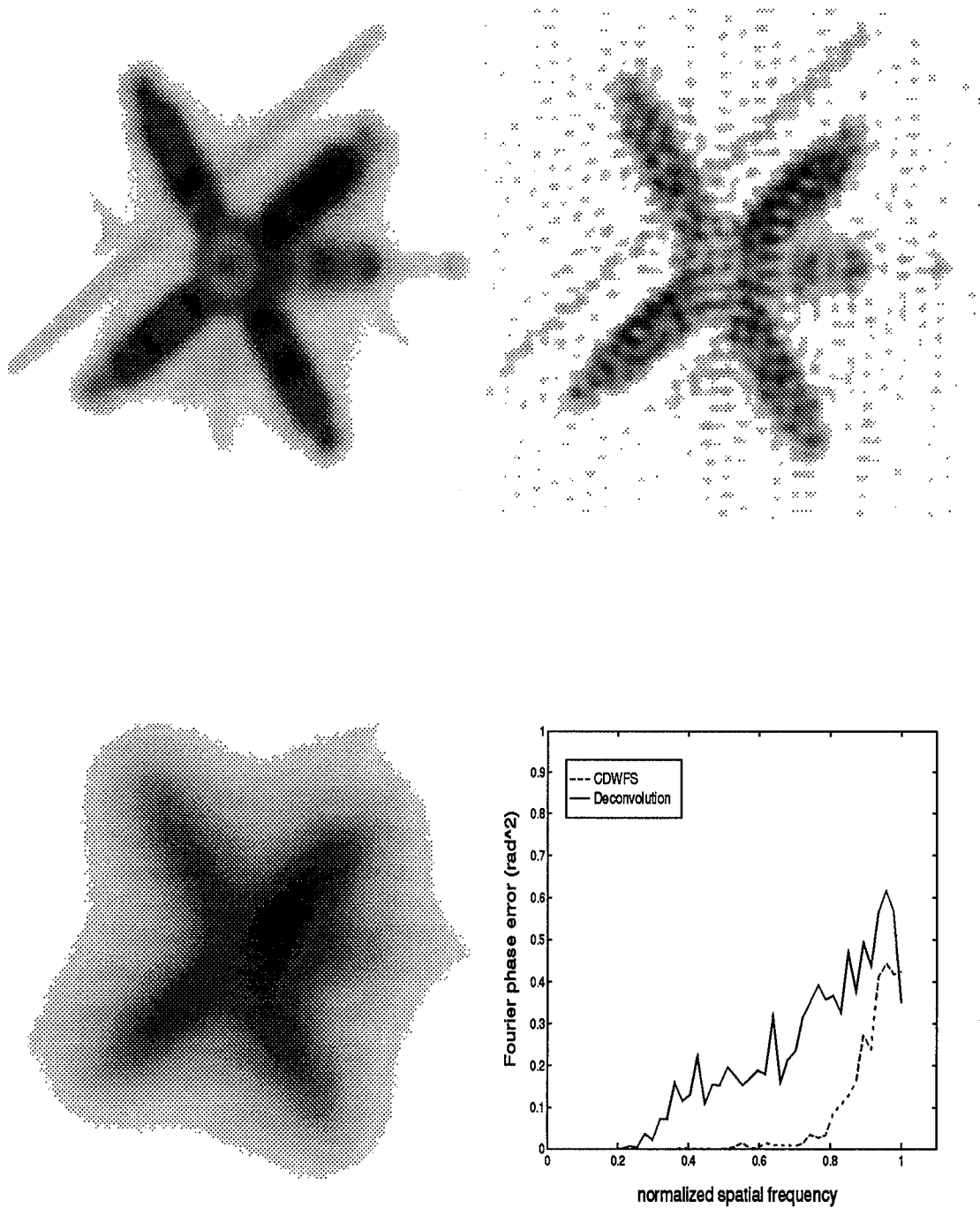


Figure 24. Average CDWFS image (top left), average deconvolved image (top right), long exposure image (bottom left), and the radially averaged mean-square Fourier phase error (bottom right) with a visual magnitude, m_ν , of 4.0 and $\bar{v}t = 0$ cm

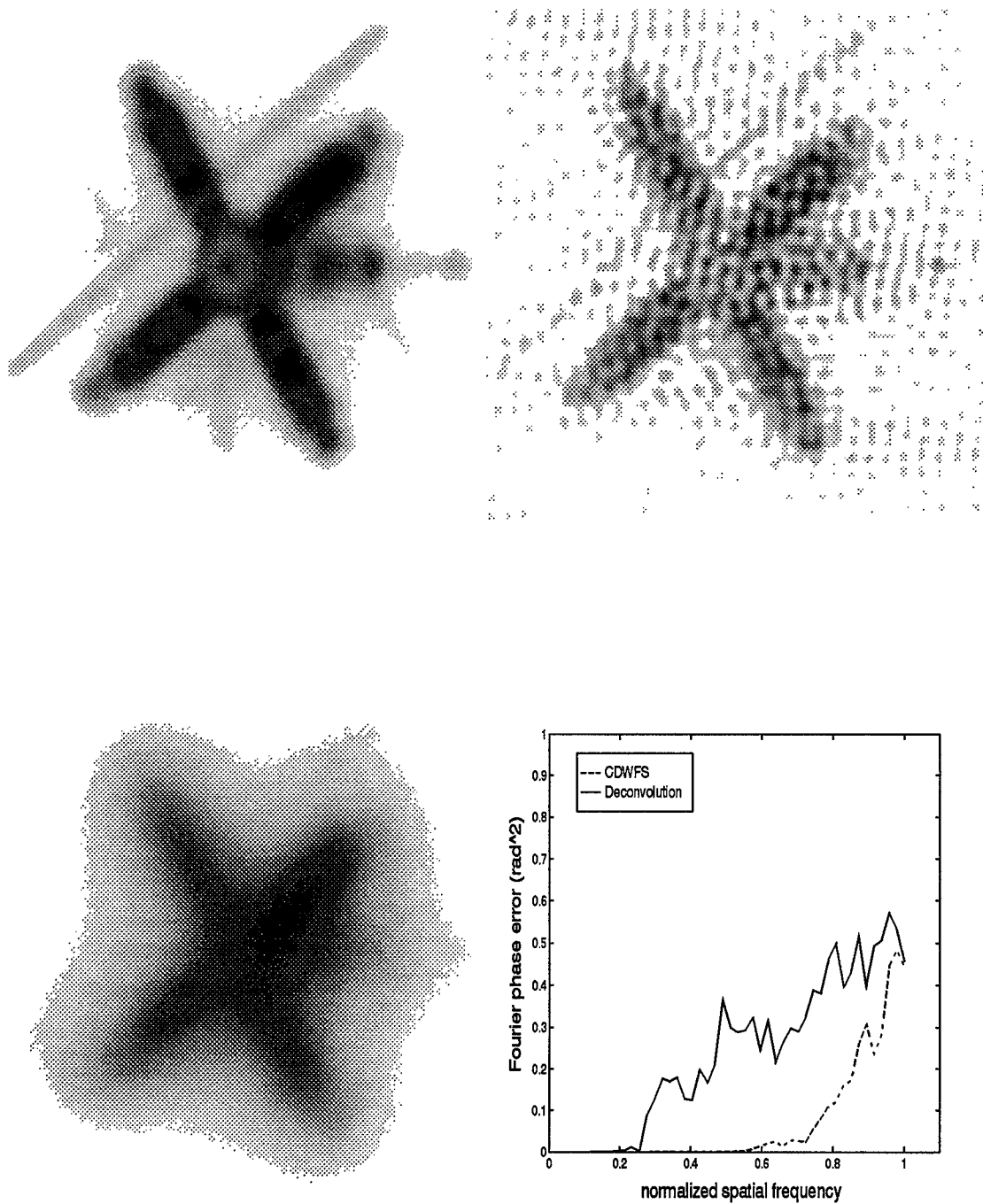


Figure 25. Average CDWFS image (top left), average deconvolved image (top right), long exposure image (bottom left), and the radially averaged mean-square Fourier phase error (bottom right) with a visual magnitude, m_v , of 5.0 and $\bar{v}t = 0$ cm

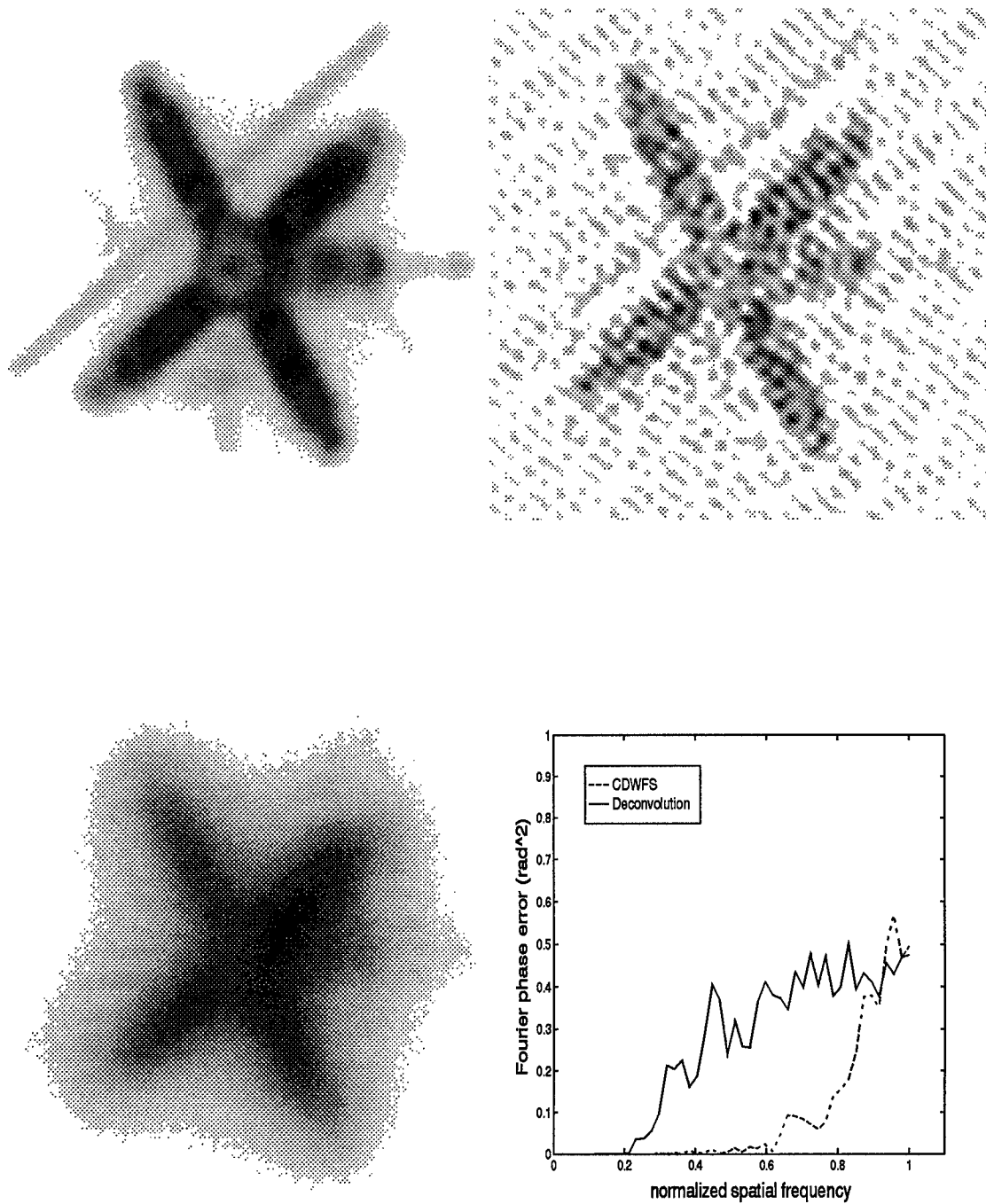


Figure 26. Average CDWFS image (top left), average deconvolved image (top right), long exposure image (bottom left), and the radially averaged mean-square Fourier phase error (bottom right) with a visual magnitude, m_v , of 6.0 and $\bar{v}t = 0$ cm

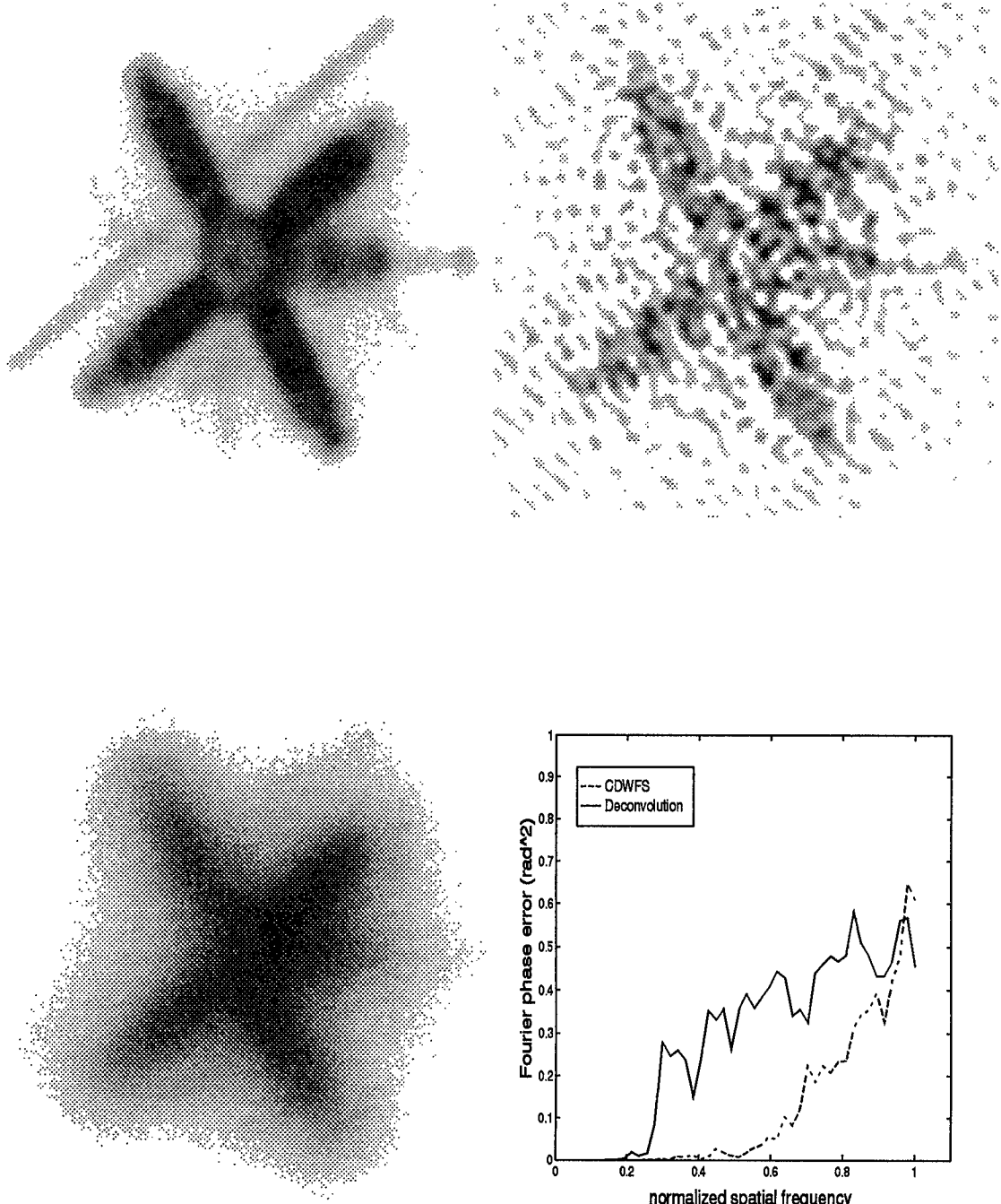


Figure 27. Average CDWFS image (top left), average deconvolved image (top right), long exposure image (bottom left), and the radially averaged mean-square Fourier phase error (bottom right) with a visual magnitude, m_ν , of 7.0 and $\vec{vt} = 0$ cm

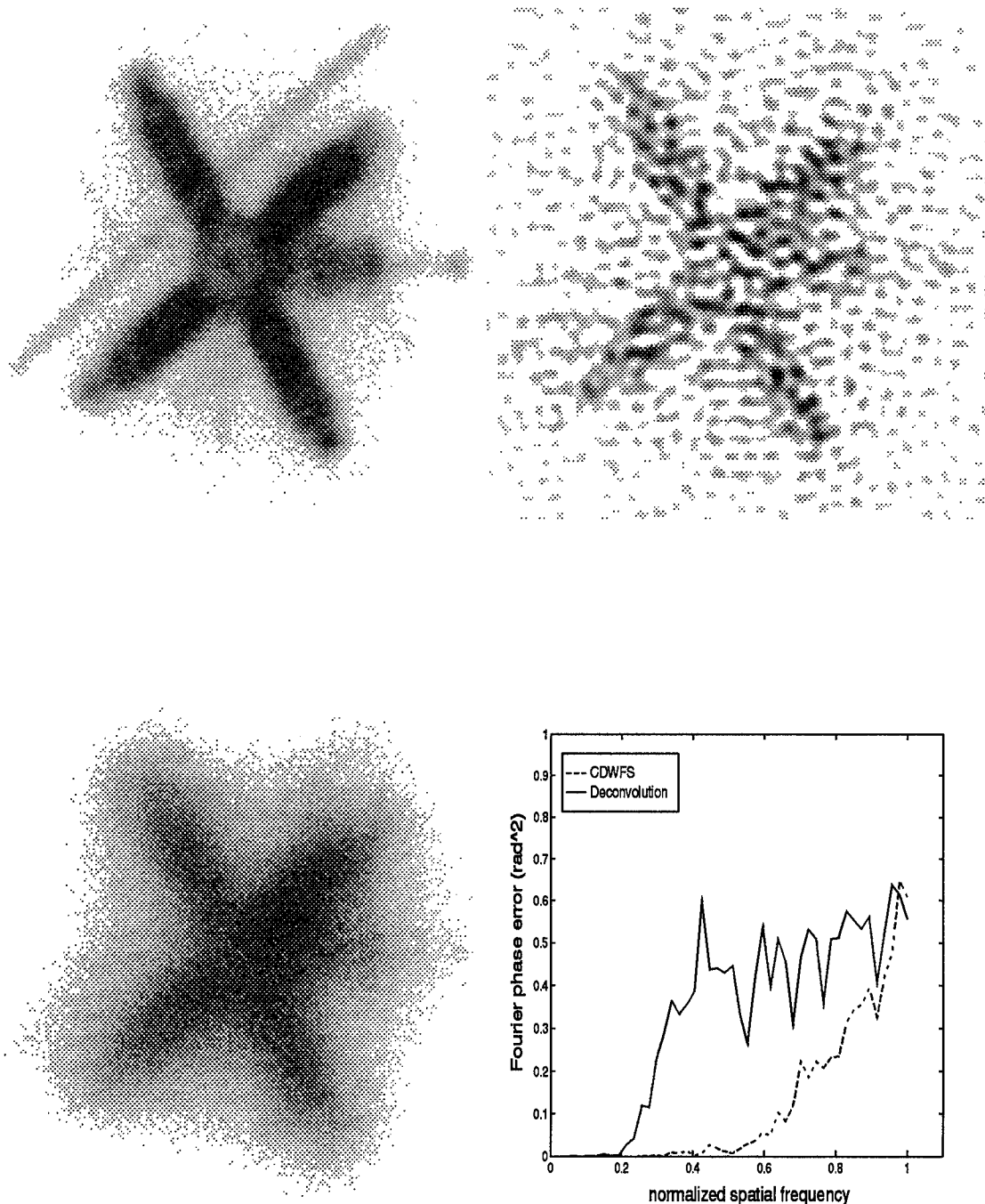


Figure 28. Average CDWFS image (top left), average deconvolved image (top right), long exposure image (bottom left), and the radially averaged mean-square Fourier phase error (bottom right) with a visual magnitude, m_v , of 8.0 and $vt = 0$ cm

4.4.3 Conclusion. This experiment investigates the use of computer generated photon values to simulate imaging of objects of various visual magnitudes. As the visual magnitude, m_ν , is increased from 0.0 to 8.0, the CDWFS results are not affected by the limited number of photons available until $m_\nu = 7.0$. The deconvolution results begin to be effected by the limited number of photons available at $m_\nu = 2.0$. Reducing the availability of photons available for image reconstruction lowers the signal and allows noise to have more of an effect. Deconvolution, however, uses an inverse filter to boost high spatial frequencies of the image and under these conditions the increased high spatial frequency noise is boosted as well. These results clearly demonstrate that the CDWFS technique is able to image much dimmer objects than the deconvolution technique. The reconstructed images provided by the CDWFS technique degrade only a fraction of the degradation seen in the reconstructed images from deconvolution.

4.5 Experiment four

This experiment investigates the performance of the CDWFS technique with respect to the visual magnitude of the object of interest, but at a time delay of 10 cm. The CDWFS technique and the conventional deconvolution technique are compared for various visual magnitudes of the object with a delay time of 10 cm.

4.5.1 Simulation Parameters. The parameter r_o is set equal to 10 cm to simulate ‘average’ seeing conditions. The time delay was set to a 10 cm. The CDWFS technique and the deconvolution technique are compared for various visual magnitudes of the object, but with a realistic time delay of 10 cm.

4.5.2 Simulation Results. This experiment investigates the use of the CDWFS technique when the visual magnitude is varied and the time delay is set to 10 cm. Figure 29 shows the results for a visual magnitude of 0.0. The CDWFS Fourier phase error yields $f_{eff} = 90\%$ and the conventional deconvolution Fourier phase error yields $f_{eff} = 47\%$. In Figure 30 the visual magnitude is set to 5.0. As expected, the deconvolved image is affected by the limited number of photons available for reconstruction. The CDWFS Fourier phase error yields $f_{eff} = 75\%$ and the conventional deconvolution Fourier phase error effective cutoff equal 40%. With a visual magnitude of 7.0, see Figure 31, the CDWFS Fourier phase error yields $f_{eff} = 65\%$ and the conventional deconvolution Fourier phase error yields $f_{eff} = 30\%$. The CDWFS image is beginning to show the effects of the limited number of photons available for reconstruction, as in experiment 3. In Figure 32, the CDWFS Fourier phase error yields $f_{eff} = 50\%$ and the conventional deconvolution Fourier phase error yields $f_{eff} = 25\%$ for a visual magnitude of 8.0. Figure 33 shows the Fourier phase errors for all four visual magnitudes for the CDWFS technique (top) and for the deconvolution technique (bottom). The CDWFS Fourier phase error degrades as the object gets dimmer. The conventional deconvolution Fourier phase error yields high Fourier phase errors for all four cases. In each of the four cases, the

CDWFS technique outperforms the deconvolution technique when the mean-square Fourier phase error is used as the metric.

4.5.3 Conclusion. This experiment investigates the CDWFS technique with respect to the visual magnitude of the object of interest, but at a time delay of 10 cm. As the visual magnitude increased from 0.0, 5.0, 7.0 and 8.0, the CDWFS technique produces images with lower mean-square Fourier phase errors in all cases. The CDWFS technique is able to image objects up to a visual magnitude of 7.0 without being affected by the limited number of photons available for reconstruction, whereas the deconvolution technique begins to be affected at lower visual magnitudes because of the boosted high spatial frequency noise.

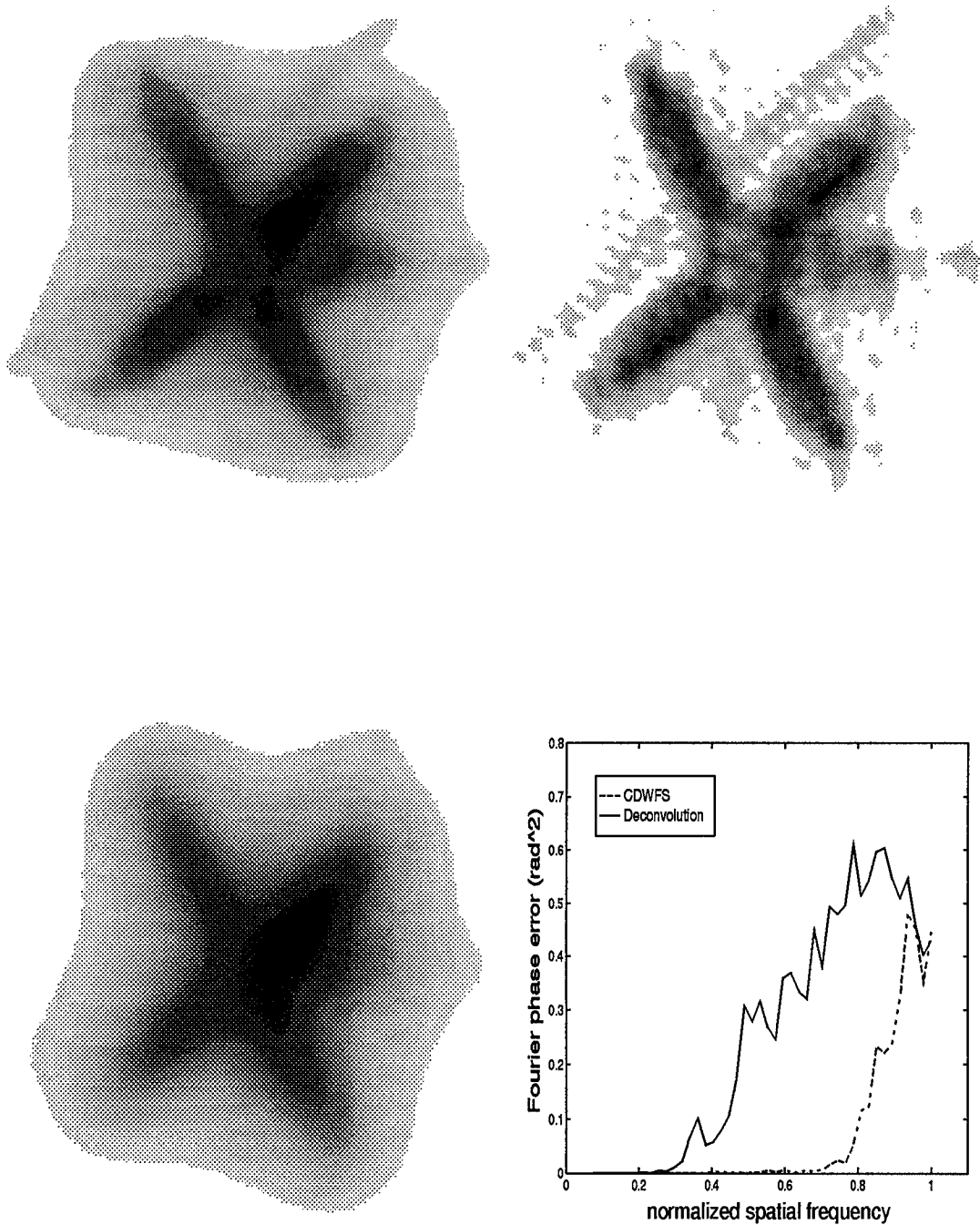


Figure 29. Average CDWFS image (top left), average deconvolved image (top right), long exposure image (bottom left), and the radially averaged mean-square Fourier phase error (bottom right) with a visual magnitude, m_ν , of 0.0 and $\bar{v}t = 10$ cm

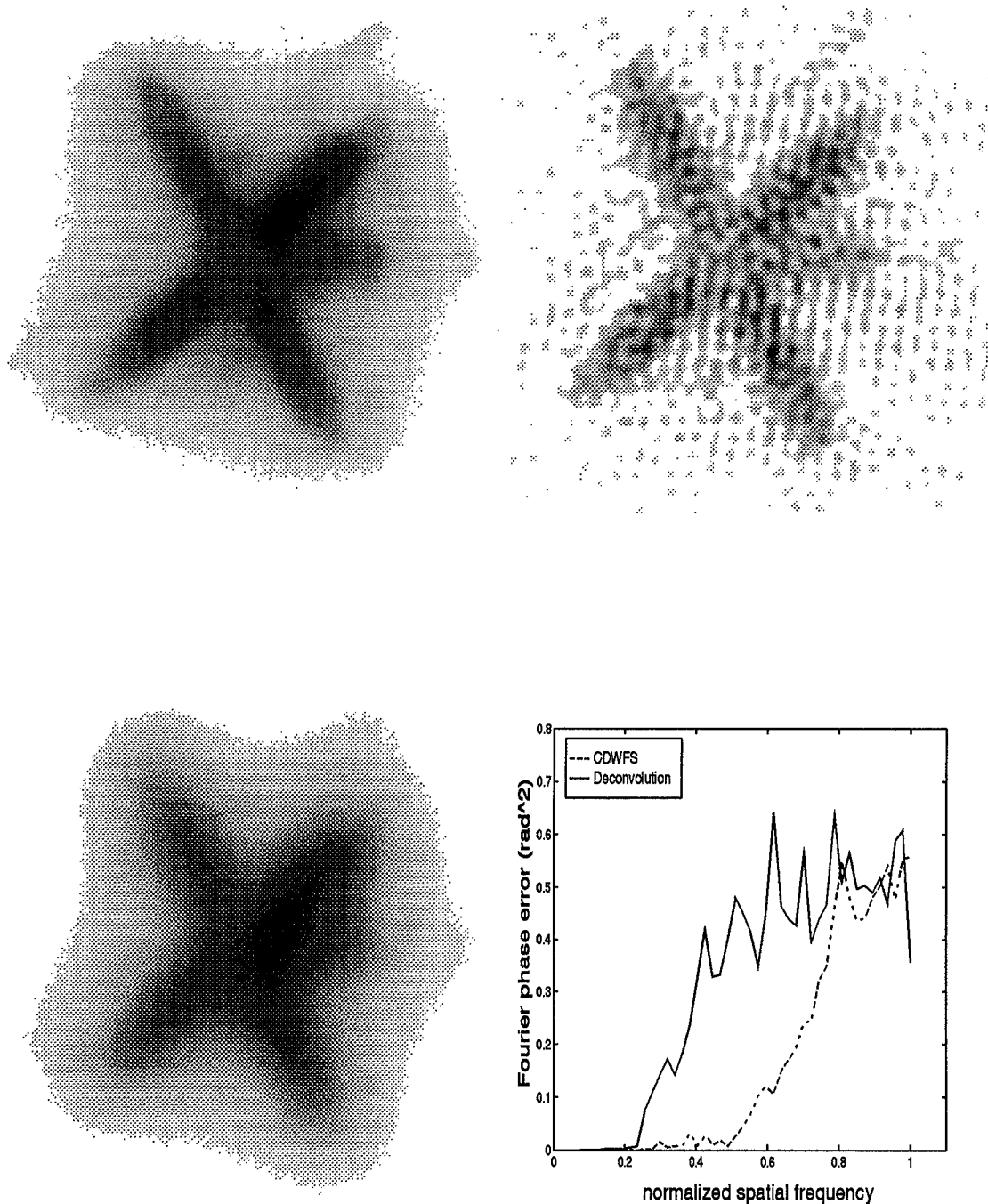


Figure 30. Average CDWFS image (top left), average deconvolved image (top right), long exposure image (bottom left), and the radially averaged mean-square Fourier phase error (bottom right) with a visual magnitude, m_v , of 5.0 and $\bar{v}t = 10$ cm

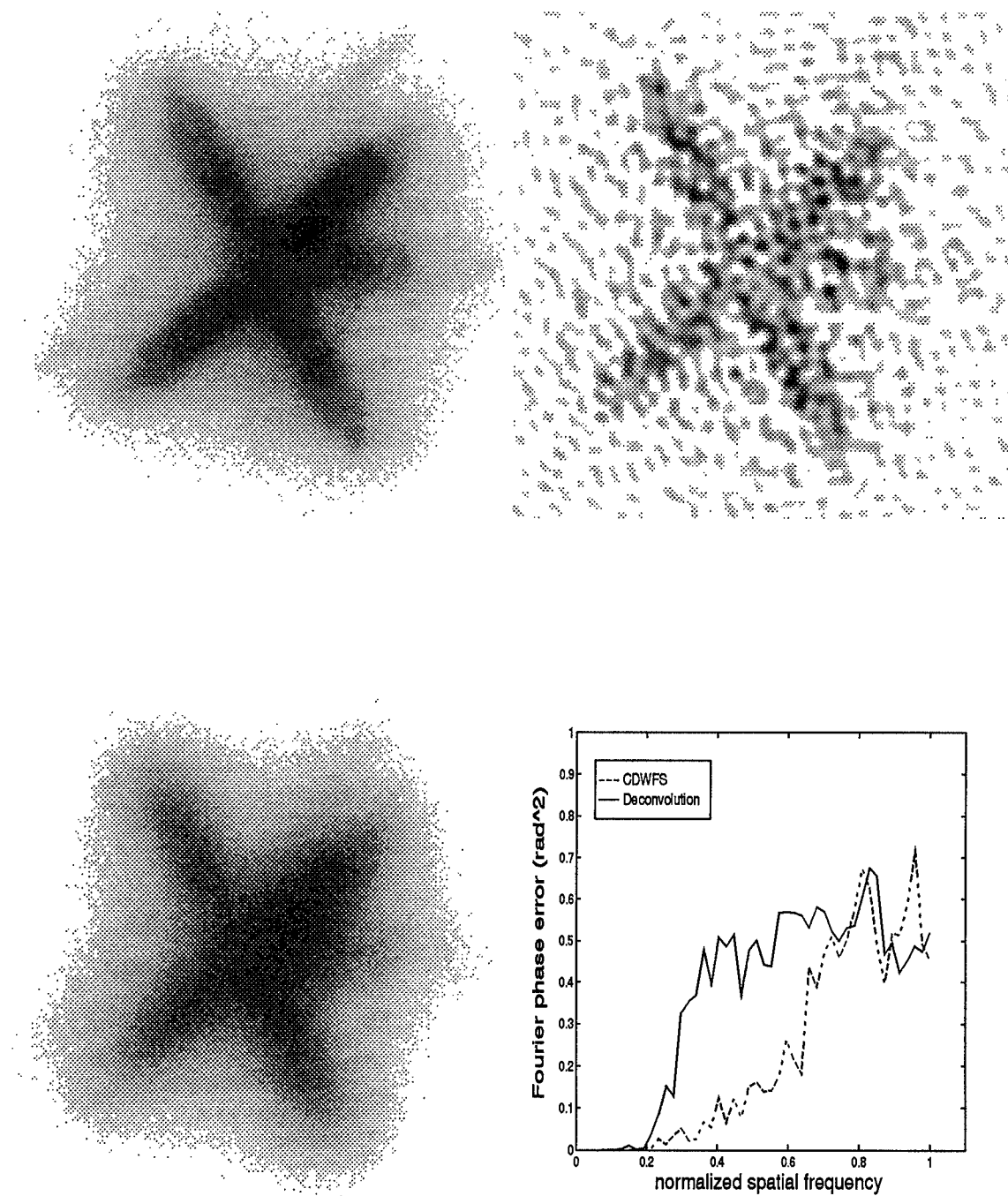


Figure 31. Average CDWFS image (top left), average deconvolved image (top right), long exposure image (bottom left), and the radially averaged mean-square Fourier phase error (bottom right) with a visual magnitude, m_v , of 7.0 and $vt = 10$ cm

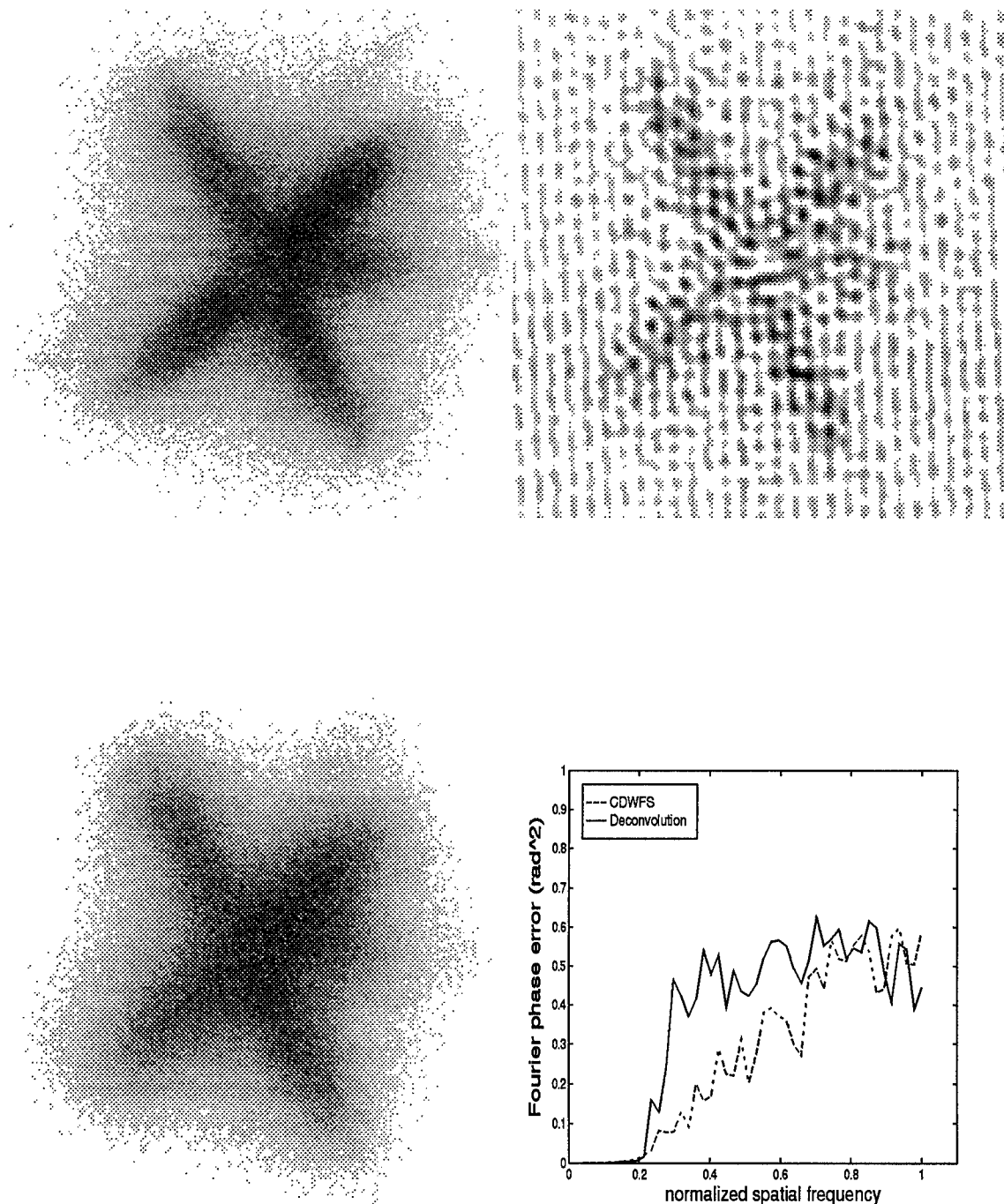


Figure 32. Average CDWFS image (top left), average deconvolved image (top right), long exposure image (bottom left), and the radially averaged mean-square Fourier phase error (bottom right) with a visual magnitude, m_v , of 8.0 and $vt = 10$ cm

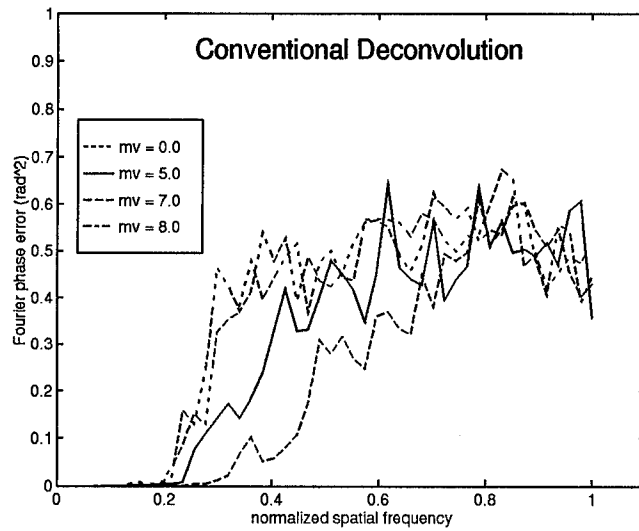
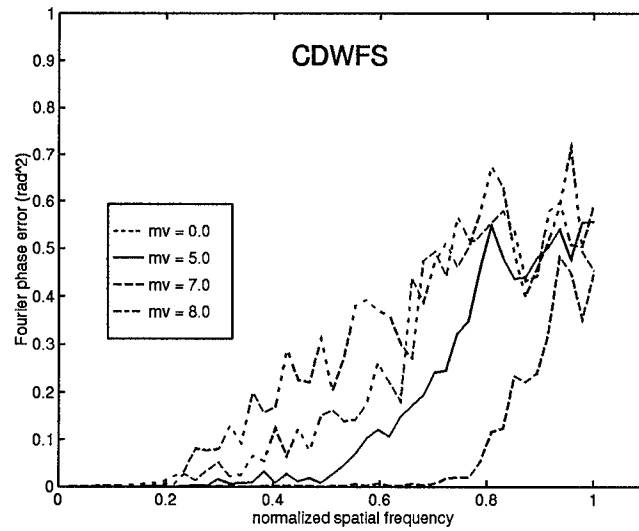


Figure 33. Radially averaged mean-square Fourier phase errors for the average CD-WFS images (top) and the deconvolution images (bottom) with visual magnitudes m_v of 0.0, 5.0, 7.0, and 8.0 and $\vec{v}t = 10$ cm

4.6 *Conclusion*

This chapter establishes that the CDWFS technique outperforms the deconvolution technique for all experiments performed when the mean-square Fourier phase error is used as the performance metric. The CDWFS technique outperforms deconvolution because deconvolution does not have an estimate of the OTF for each realization and therefore relies on an average OTF to reconstruct images. Deconvolution also uses an inverse filter to try to boost high spatial frequencies because the telescope-adaptive optics-atmosphere system highly attenuates high spatial frequencies. In attempting to boost these high spatial frequencies, deconvolution also boosts high spatial frequency noise. This effect is seen in the images generated by deconvolution. The CDWFS technique provides an estimate of the OTF for each realization thereby eliminating the need for the inverse filter and preventing the injecting of the high spatial frequency noise. The CDWFS technique also allows dimmer objects to be imaged because the longer delay times allow longer integration times in the WFS which then leads to reducing the operational bandwidth.

V. Conclusions and Recommendations

5.1 Introduction

The motivation for this thesis stems from the Air Force mission to obtain imagery of earth-orbiting objects. Previous results [14] have shown with star imagery that the CDWFS technique improves performance when the delay times in the closed-loop system becomes large and when the seeing conditions become "poor". This thesis extends the previous work by incorporating extended object imaging and by incorporating objects with various visual magnitudes. This chapter presents a brief summary of what was accomplished by this research effort and provides recommendations for future research into this area.

5.2 Conclusions

1. The CDWFS technique allows longer delay times in the closed-loop system while providing reconstructed images that increase the mean-square Fourier phase error only slightly. The use of longer delay times implies that the bandwidth of operation can be reduced. This reduction of the closed-loop bandwidth permits longer integration times in the WFS, which then allows dimmer objects to be imaged without the use of an artificial guidestar.

2. The CDWFS technique outperforms deconvolution under 'poor' seeing conditions for all time delays investigated here when the mean-square Fourier phase error is used as the performance metric. The CDWFS technique provides low mean-square Fourier phase errors under 'poor' seeing conditions, whereas deconvolution introduces high mean-square Fourier phase error at all time delays.

3. The CDWFS technique outperforms deconvolution when the visual magnitude of the object is increased from 0.0 to 8.0. The CDWFS technique shows no sign of degradation due to the limited number of photons available for reconstruction for visual magnitudes of 6.0 and below. Deconvolution shows no sign of degradation due

to the limited number photons available for reconstruction for visual magnitudes of 2.0 and below. These results prove once again that the CDWFS technique can image dimmer objects without the use of an artificial guidestar.

4. The CDWFS technique produces reconstructed images with lower mean-square Fourier phase errors when compared to deconvolution for various visual magnitudes at a realistic time delay of 10 cm. The use of the WFS measurements in the reconstruction process improves the optical performance as measured by the mean-square Fourier phase error performance metric.

5. The CDWFS technique outperforms deconvolution because deconvolution does not have an estimate of the OTF for each realization and therefore relies on an average OTF to reconstruct images. Deconvolution also uses an inverse filter to try to boost high spatial frequencies because the telescope-adaptive optics-atmosphere system highly attenuates high spatial frequencies. In boosting these high spatial frequencies, it also boost high spatial frequency noise. This effect is seen in the images generated by deconvolution. The CDWFS technique provides an estimate of the OTF for each realization thereby eliminating the need for the inverse filter and preventing the injecting of the high spatial frequency noise.

6. An important point that was not considered when obtaining the simulation results, was the fact that the WFS should operate at a sampling rate of $10\times$ the closed-loop bandwidth of the system for stability reasons [14]. The photon values were obtained for a fixed WFS sampling rate of 3.33 ms and a fixed imaging integration time of 10 ms. For each delay time, \vec{vt} , the WFS should operate at $10\times$ the closed-loop bandwidth providing WFS integration times of 0 sec, 0.9 ms, 1.8 ms and 3.6 ms for each 0 cm, 5 cm, 10 cm and 20 cm delay time, respectively. Using these values in calculating the photon values would provide results more closely related to actual operating conditions.

5.3 Recommendations for Further Research

The simulation results show that the CDWFS technique provides better results when compared to conventional deconvolution when the mean-square Fourier phase error is used as the performance metric. The next step in evaluating the CDWFS technique is to do experimental testing of the technique. The capability now exists at Phillips Laboratory Starfire Optical Range (SOR) for conducting experiments to validate the theory and expose the next layer of questions regarding partially compensated satellite imaging systems.

The CDWFS results could be compared against the DWFS technique to see how much improvement is obtained. Simulation upgrades could be an area of further research, as well. Specifically, CCD read noise in the WFS and in imagery and multi-layered turbulence could be incorporated to give that better model the real world applications.

Bibliography

1. H.W. Babcock, "The possibility of compensating astronomical seeing", *Publ. Astron. Soc. Pac.*, 65:229-236, 1953.
2. D.L. Fried, "Optical resolution through a randomly inhomogeneous medium for very long and very short exposures", *Journal of the Optical Society of America*, 56(10):1372-1379, 1966.
3. R.Q. Fugate, B.L. Ellerbroek, C.H. Higgins, M.P. Jelonek, W.J. Lange, A. C. Slavin, W. J. Wild, D. M. Winker, J. M. Wynia, J. M. Spinhirne, B.R. Boeke, R.E. Ruane, J.F. Moroney, M.D. Oliker, D.W. Swindle, and R.A. Cleis, "Two generations of laser guide star adaptive optics experiments at the Starfire Optical Range," *JOSA-A*, 11:310-324, 1994.
4. J.D. Gonglewski, D.G. Voelz, J.S. Fender, D.C. Dayton, B.K. Spielbusch, and R.E. Pierson, "First astronomical application of postdetected turbulence compensation: images of α Aurigae, ν Ursa Majoris, and α Geminorum using self-referenced speckle holography", *J. Appl. Opt.*, 29:4527-4529, 1990.
5. J.W. Goodman, *Introduction to Fourier Optics*, McGraw-Hill, New York, 1968.
6. J.W. Goodman, *Statistical Optics*, Wiley-Interscience Publications, New York, 1985.
7. J.W. Hardy, "Active optics: a new technology of the control of light", *Proc. IEEE*, 66:651-697, 1978.
8. J.W. Hardy, "Adaptive Optics - a progress review", *Proc. SPIE on Active and Adaptive Optical Systems*, 1542:2-17, 1991.
9. P.S. Idell and A. Webster, "Resolution limits for coherent optical imaging: signal-to-noise analysis in the spatial frequency domain," *J. Opt. Soc. Am. A*, 9:43-56, 1992.
10. J. Primot, G. Rousset, and J.C. Fontanella, "Deconvolution from wave-front sensing: a new technique for compensating turbulence-degraded images", *J. Opt. Soc. Am. A*, 7:1598-1608, 1990.
11. F. Roddier, "The effects of atmospheric turbulence in optical astronomy," *Progress in Optics XIX*, 1981.
12. F. Roddier, "The effects of atmospheric turbulence in optical astronomy", *Progress in Optics XIX*, edited by E. Wolf, North-Holland, Amsterdam, pages 283-378, 1981.
13. F. Roddier, M. Northcott and J.E. Graves, "A simple low-order adaptive optics system for near-infrared applications", *Publ. Astron. Soc. Pac.*, 103:131-149, 1991.

14. M. C. Roggemann and J. A. Meinhardt, "Image reconstruction by means of wave-front sensor measurements in closed-loop adaptive-optics systems", *J. Opt. Soc. Am. A*, 10:1996-2007, 1993.
15. M.C. Roggemann, "Limited degree-of-freedom adaptive optics and image reconstruction", *Appl. Opt.*, 30:4227-4233, 1991.
16. M.C. Roggemann, D.W. Tyler, and M.F. Bilmont, "Linear reconstruction of compensated images: theory and experimental results", *J. Appl. Opt.*, 17:7429-7441, 1992.
17. M.C. Roggemann, "Optical performance of fully and partially compensated adaptive optics systems using least-squares and minimum variance phase reconstructors," *Comput. Electr. Eng.*, 18:451-466, 1992.
18. M.C. Roggemann and C.L. Matson, "Power spectrum and Fourier phase spectrum estimation using fully and partially-compensating adaptive optics and bispectrum postprocessing", *J. Opt. Soc. Am. A*, 9:1525-1535, 1992.
19. M.C. Roggemann, B.L. Ellerbroek, and T.A. Rhoadarmer, "Widening the effective field-of-view of adaptive optics telescopes using deconvolution from wave-front sensing: average and signal-to-noise ratio performance," submitted to *JOSA-A*, December 1993.
20. R.C. Smithson and M.L. Peri, "Partial correction of astronomical images with active mirrors", *J. Opt. Soc. Am. A*, 6:92-97, 1989.
21. R.E. Wagner, "Post-processing of imagery from active optics - some pitfalls", *Imaging Through the Atmosphere 75*, edited by James E. Wyant, 136-140, SPIE, Palos Verdes Estates, California, 1976.
22. E.P. Wallner, "Optimal wave-front correction using slope measurements," *JOSA-A*, 73:1771-1776, 1983.
23. J.Y. Wang and J.K. Markley, "Modal compensation of atmospheric turbulence phase distortion", *J. Opt. Soc. Am. A*, 68:78-87, 1978.
24. B.M. Welsh and C.S. Gardner, "Performance analysis of adaptive-optics systems using laser guide stars and slope sensors", *Journal of the Optical Society of America A*, 6(12):1913-1923, December 1989.
25. B.M. Welsh and R.N. VonNiederhausern, "Performance analysis of self-referenced speckle holography", *Atmospheric Propagation and Remote Sensing*, A. Kohnle and W. B. Miller, eds., Proc. Soc. Photo-Opt. Instrum. Eng., 1688:572-582, 1992.

Vita

Lieutenant Lori A. Thorson was born on 22 April 1970 in Sioux City, Iowa. She graduated from Gibbon Public High School in 1988 and entered the University of Nebraska-Lincoln. She graduated from the University of NE-Lincoln with a Bachelor of Science in Electrical Engineering and a commission in the USAF, and was selected to attend the School of Engineering, Air Force Institute of Technology.

Permanent address: 64 Lakeshore Drive
Spring Valley, OH 45370

REPORT DOCUMENTATION PAGE

Form Approved
OMB No. 0704-0188

Public reporting burden for this collection of information is estimated to average 1 hour per response, including the time for reviewing instructions, searching existing data sources, gathering and maintaining the data needed, and completing and reviewing the collection of information. Send comments regarding this burden estimate or any other aspect of this collection of information, including suggestions for reducing this burden, to Washington Headquarters Services, Directorate for Information Operations and Reports, 1215 Jefferson Davis Highway, Suite 1204, Arlington, VA 22202-4302, and to the Office of Management and Budget, Paperwork Reduction Project (0704-0188), Washington, DC 20503.

1. AGENCY USE ONLY (Leave blank)		2. REPORT DATE December 1994	3. REPORT TYPE AND DATES COVERED Master's Thesis	
4. TITLE AND SUBTITLE Compensated Deconvolution from Wavefront Sensing			5. FUNDING NUMBERS	
6. AUTHOR(S) Lori A. Thorson				
7. PERFORMING ORGANIZATION NAME(S) AND ADDRESS(ES) Air Force Institute of Technology, WPAFB OH 45433-6583			8. PERFORMING ORGANIZATION REPORT NUMBER AFIT/GE/ENG/94D-29	
9. SPONSORING / MONITORING AGENCY NAME(S) AND ADDRESS(ES) Dr. Brent Ellerboek Phillips Laboratory/LIG 3550 Aberdeen Ave., SE Kirtland AFB, OH 87117-3556			10. SPONSORING / MONITORING AGENCY REPORT NUMBER	
11. SUPPLEMENTARY NOTES				
12a. DISTRIBUTION / AVAILABILITY STATEMENT Distribution Unlimited			12b. DISTRIBUTION CODE	
13. ABSTRACT (Maximum 200 words)				
<p style="text-align: center;">Abstract</p> <p>The U.S. Air Force has a continuing mission to obtain imagery of earth-orbiting objects. One of the means for obtaining this imagery is through the use of ground-based observatories. A fundamental problem associated with imaging objects through the atmosphere is that atmospheric turbulence inflicts a large, random aberration on the telescope which effectively limits the realizable resolution to that of a much smaller telescope. Several approaches have been taken to overcome these effects including pure post processing, pure adaptive optics, and hybrid techniques involving both adaptive optics and image post processing. One key result from past approaches is that partially compensated systems can be used in conjunction with image processing to overcome most of the optical effects of atmospheric turbulence while retaining nearly the performance of a fully compensated system. One hybrid approach is compensated deconvolution from wavefront sensing (CDWFS). This method uses wavefront sensor measurements in conjunction with short exposure images to improve the effective optical performance. This thesis formulates and executes a plan which allows fundamental questions regarding partially compensated adaptive optics performance to be answered. Specifically, imaging of extended objects using the CDWFS technique is investigated, through simulation. The simulation results demonstrate that the CDWFS technique can be used to reduce the required closed-loop bandwidth of an imaging system, permitting longer integration times in the wavefront sensor, and thus allowing dimmer objects to be imaged without the use of an artificial guidestar.</p>				
14. SUBJECT TERMS Partially compensated imaging technique, Extended object imaging, Deconvolution			15. NUMBER OF PAGES 88	
			16. PRICE CODE	
17. SECURITY CLASSIFICATION OF REPORT UNCLASSIFIED	18. SECURITY CLASSIFICATION OF THIS PAGE UNCLASSIFIED	19. SECURITY CLASSIFICATION OF ABSTRACT UNCLASSIFIED	20. LIMITATION OF ABSTRACT UL	